BETA-NEUTRINO ANGULAR CORRELATIONS IN THE DECAY OF ^{33}AR

by

Thomas Charles Spencer

A dissertation submitted to the faculty of The University of North Carolina at Chapel Hill in partial fulfillment of the requirements for the degree of Doctor of Philosophy in the Department of Physics and Astronomy.

Chapel Hill

1990

Approved by:

_____

Advisor

_____

Reader

_____

Reader

THOMAS CHARLES SPENCER. Beta-neutrino angular correlations in the decay of ^{33}Ar. (Under the direction of HUGON J. KARWOWSKI.)

Abstract

Interest in the β–ν angular correlation stems from the dependence of the correlation coefficient (a) on the behavior of the β-decay interaction hamiltonian under Lorentz transformations. Present upper limits on the ratio of the strengths of the scalar and vector interaction terms (5% at the 95% confidence level) and the ratio of the tensor and axial-vector strengths (0.7% at 95% CL) result primarily from measurements of a for various nuclear systems.

A new determination of a for the decay of the β-delayed proton emitter ^{33}Ar to the ground state analog level in ^{33}Cl has been performed by measuring the energies of protons detected in coincidence with positrons. The average lab-frame energy of the protons depends on the average recoil velocity of the ^{33}Cl atom, which is in turn a function of a for a given positron momentum. This decay branch proceeds primarily through the Fermi (vector or scalar) interaction, with a small Gamow-Teller (axial-vector or tensor) contribution. An upper limit on the scalar-to-vector strength ratio is then obtained. The results also permit an upper limit on the nuclear Gamow-Teller matrix element to be obtained. The magnitude of this matrix element is sensitive to the form and magnitude of the nuclear isospin symmetry breaking interactions and therefore provides a constraint on the construction of nuclear interaction models.

Abstract ii
List of Figures iii
List of Tables vi
Chapter 1. The Weak Interaction and Nuclear Beta Decay. 1
1.1. Introduction 1
1.2. The Standard Model of Electroweak Interactions. 1
1.3. Current-Current Interactions. 6
1.4. Nuclear Structure and Beta Decay 10
1.5. Experimental Limits on the Interaction Amplitudes. 15
Chapter 2. The Beta-neutrino Angular Correlation Coefficient. 21
2.1. Introduction 21
2.2. $\beta - \nu$ Correlation. 21
2.3. β - delayed Particle Emission and Decay of ^{33}Ar 24
2.4. Effective Coupling Constants 31
2.5 Isospin 35
2.6. The Nuclear Shell Model and GT Transition Strengths 38
2.7. Summary 40
Chapter 3. Experimental Equipment and Procedures 42
3.1. Introduction 42
3.2. ^{33}Ar Production and Transport. 42
3.3. Detector Geometry and Detection Electronics 48
3.4 Detector Calibration. 56
3.6. Conclusion. 72
Chapter 4. Data Analysis. 78
4.1. Introduction 78
4.2. Data Reduction. 78
4.3. Monte Carlo Simulation 80
4.4. Comparison of the Calculations and Data. 92
4.5. Conclusions. 97
Chapter 5. Discussion. 99
5.1. The Measurement of a. 99
5.2. Isospin Mixing in ^{33}Cl 100
5.3. Speculations on Future Research. 101
References 108

LIST OF FIGURES

Figure 1.1. Feynman diagrams for nuclear beta decay processes in both the effective theory and the standard model. 8

Figure 1.2. Decay geometry for both the axial vector and tensor interactions. 17

Figure 2.1. Simplified ^{33}Ar decay scheme. 26

Figure 2.2 Proton energy shifts as a function of positron energy. 29

Figure 3.1. The ^{33}Ar production and transport system. 43

Figure 3.2. The counting chamber setup. 49

Figure 3.3. Schematic of the detection electronics. 51

Figure 3.4. Proton singles spectrum. 56

Figure 3.5 Scattering chamber setup for mylar foil thickness measurements. 58

Figure 3.6. Detemination of energy loss of 3.2 MeV protons in the mylar foil. 59

Figure 3.7. Gain shifts for surface barrier detectors one and four. 60

Figure 3.8. Kurie plot of the positron spectrum of ^{33}Ar 63

Figure 3.9. The Compton electron energy spectrum as determined by Monte Carlo modeling. 65

Figure 3.10. Modified Kurie plot of ^{33}Ar for detector 4. 66

Figure 3.11. The calibration of beta counter 4. 69

Figure 3.12. Modified Kurie plots of spectra acquired to determine the scintillator response function. 70

Figure 3.13. The energy calibration of the scintillation detector used to determine the response of the telescopes to positrons. 71

Figure 3.14. The scintillation detector response to positrons. 72

Figure 3.15. Fits to the positron spectra of ^{19}Ne, ^{23}Mg, and ^{27}Si. 75

Figure 4.1. Logic flowchart of the data sorting program. 79

Figure 4.2. Experimental proton energy shifts as a function of beta-particle energy bin. 81

Figure 4.3. The logic of the Monte Carlo simulation. 84

Figure 4.4. Example of the dependence of the calculated proton energy shifts on beta-particle energy and correlation coefficient. 86

Figure 4.5. A comparison of the proton energy shifts produced by the Monte Carlo simulation for three different beta energy spectra. 89

Figure 4.6. Comparison of proton energy shifts calculated for point and extended source geometry. 90

Figure 4.7. The effect of a realistic detector response function on the proton energy shifts. 91

Section 4.8. Calculated proton energy shifts for different counting cell wall thicknesses. 93

Figure 4.9. Detected and calculated positron energy spectra. Each bin corresponds to a 150 keV range of positron energy. 94

Figure 4.10 Calculated proton energy shifts for several values of a and the experimental results. 95

Figure 4.11. Chi-squared per point for various values of the angular correlation coefficient. 96

LIST OF TABLES

Table 1.1 The quantities used in Paul's fit to the transition amplitudes C_i. 20

Table 2.1. The beta neutrino angular correlation coefficient for the lowest order decay class produced by each of the five possible weak interaction terms. 22

Table 3.1. Parent nuclei, transition energy, and Compton edge energy of the transitions used to monitor the scintillation detector gains. 62

Table 3.2. Daughter nuclei, positron endpoint energies, and branching ratios of the transitions used to determine the response function of the scintillation detectors. 68

Table 4.1. Experimental proton energy shifts for each positron energy bin. 81

Table 4.2. The results of the simplified Monte Carlo simulation of the experiment compared with the analytic calculation of the shift. 88

Table 4.3. The chi-squared per point of the Monte Carlo results for several values of the angular correlation coefficient. 97

Table 5.1. Delayed proton particle emitters with A < 45. 107

Table 5.2. Delayed alpha particle emitters with A < 45. 8Li, 12B, and 16N are electron emitters, all other isotopes decay by positron emission. 107

Table 5.3. Delayed particle emitters which may be useful for determining K_{SS}/K_{VV}. 108

Chapter 1. The Weak Interaction and Nuclear Beta Decay. 1
1.1. Introduction 1
1.2. The Standard Model of Electroweak Interactions. 1
1.3. Current-Current Interactions. 6
1.4. Nuclear Structure and Beta Decay 10
1.5. Experimental Limits on the Interaction Amplitudes. 15
Chapter 2. The Beta-neutrino Angular Correlation Coefficient. 21
2.1. Introduction 21
2.2. b - n Correlation. 21
2.3. b - delayed Particle Emission and Decay of 33Ar. 24
2.4. Effective Coupling Constants 31
2.5 Isospin 35
2.6. The Nuclear Shell Model and GT Transition Strengths 38
2.7. Summary 40
Chapter 3. Experimental Equipment and Procedures 42
3.1. Introduction 42
3.2. 33Ar Production and Transport 42
3.3. Detector Geometry and Detection Electronics 48
3.4 Detector Calibration. 56
3.6. Conclusion. 72
Chapter 4. Data Analysis and Discussion 78
4.1. Introduction 78
4.2. Data Reduction. 78
4.3. Monte Carlo Simulation 80
4.4. Extraction of Centroids from the Spectra 91
4.5. Comparison of the Calculations and Data. 98
4.6. Conclusions 101
Chapter 5. Discussion and Conclusions. 104
5.1. The Measurement of a. 104
5.2. Conclusions. 105
References 106

Chapter 1. The Weak Interaction and Nuclear Beta Decay.

Section 1.1. Introduction.

The study of the weak interaction began at the end of the nineteenth century with Becquerel's discovery of radioactivity (Bec96) and demonstration that beta rays are electrons (Bec00). Explaining the many puzzles of weak interaction processes drove many important innovations in theoretical particle physics, culminating during the 1960's with the development of a phenomenological gauge theory, now known as the standard model of electroweak interactions, which unifies the weak and electromagnetic interactions (Gla61, Sal64, Wei67, Gla70, Wei70).

The project described in this thesis was undertaken to search for a scalar interaction contributing to nuclear beta decay. The presence of a scalar current would indicate that the standard model is not a complete description of the weak interaction. This chapter provides a brief review of the standard model and the limits which have been placed on the form of the weak interaction by established experimental results.

Section two of this chapter presents a brief summary of the standard model of electroweak interactions. Section three describes the traditional current-current beta-decay interaction and places this theory in the more general context of the standard model. Section four contains a discussion of the nuclear structure aspects pertaining to beta-decay and the beta-decay classification scheme. The chapter closes with a summary of the experimental evidence supporting the "V-A law" which is built into the standard model and restricts the parameters of the current-current theory.

Section 1.2. The Standard Model of Electroweak Interactions.

For the past 20 years all results from weak interaction experiments have been interpreted and explained in the context of the standard model. The model has been treated thoroughly in many texts (Hal84, Com83, Geo84, in increasing order of sophistication), so only the most important aspects of the theory relevant to the present work will be summarized here.

The standard model is a Lorentz invariant quantum gauge field theory which describes the weak and electromagnetic interactions of two types of elementary particles: fermions and bosons. The fermions are, loosely speaking, the matter particles. They have spin 1/2 and therefore their motion must be described by the Dirac equation to satisfy Lorentz invariance. The bosons mediate the interactions and have integral spin. The elementary particles in the standard model include twelve fermions (and their distinct antiparticles) and four vector (spin 1) gauge bosons.

The vector bosons result from quantization of gauge fields in nearly the same manner as the photon emerges from the quantized electromagnetic potential in quantum electrodynamics. The principal difference is that some of the electroweak bosons have nonzero mass. The straightforward method of producing particle masses, by merely adding mass terms to the hamiltonian, results in a theory which is not renormalizable. That is, calculations of matrix elements require an infinite series of adjustments (renormalizations) and thus the theory cannot be employed to make predictions of transition amplitudes. To provide particle masses in a renormalizable theory, an additional gauge field is added to the hamiltonian. This field is called a Higgs field; its quanta are Higgs bosons (Hig64). The standard model includes one scalar (spin 0) Higgs boson, which has thus far evaded direct experimental detection.

The gauge bosons which mediate the electroweak interactions have spin one and may therefore produce only vector and/or axial vector interactions. Interactions which have

other symmetry properties under Lorentz transformations, such as scalar, pseudoscalar, or tensor interactions, are forbidden by the absence of mediating bosons which do not have spin one. (The Higgs boson would mediate a scalar interaction; however, the effective coupling of the interaction for processes with a momentum exchange less than the Higgs mass is expected to be much smaller than the weak coupling, assuming the Higgs boson mass is much greater than the W boson mass.)

The four vector bosons are the photon, Z^o, W^+_L and W^-_L. The photon mediates the electromagnetic interaction and is identical to the photon of quantum electrodynamics. The W^+_L and W^-_L have a mass of about 83 GeV and are responsible for the charge-exchange weak interaction. The subscript L indicates that these bosons operate only on 'left-handed' (negative helicity) fermions. In other words, the W_L bosons act only on the components of the particle spinors which have momentum and angular momentum vectors anti-aligned. The Z^o has a mass of 92 GeV and produces the neutral current (non-charge exchange) weak interaction. The Z^o acts on both left- and right-handed fermions, but with unequal strength.

The twelve fermions are divided into two classes and three generations. The division into classes is made according to whether the particles have color charge and thus are subject to strong interactions. The six 'colorless' fermions are known as leptons. The leptons are the electron (e), muon (μ), and tau lepton (τ) and their associated massless neutrinos. The first three particles have electric charge -1 and are arranged into three generations with the neutrinos according to the following diagram:

$$\left|\begin{matrix}\nu_e \\ e\end{matrix}\right| \qquad \left|\begin{matrix}\nu_\mu \\ \mu\end{matrix}\right| \qquad \left|\begin{matrix}\nu_\tau \\ \tau\end{matrix}\right|$$

The strongly interacting fermions are the quarks which are also arranged into three generations as follows:

up	charm	top
down	strange	bottom

The upper quarks in each pair have charge +2/3, the lower quarks have charge -1/3.

Both the left-handed quarks and left-handed leptons of each generation are placed in a weak isospin doublet. The W bosons are represented mathematically by the weak isospin raising and lowering operators which flip the weak isospin of the fermion spinors they act upon, thereby converting the lower particle in each doublet into the upper particle or vice versa. This is analogous to the role of the charged pions in low energy nuclear physics which are represented by the nuclear isospin raising and lowering operators that act on the neutron and proton spinors. The right-handed fermions are isosinglets. They do not interact with the W field, only the Z and γ fields.

Conservation laws for several quantities are built into the standard model. The model conserves the total energy, momentum, angular momentum, and electric charge. Mechanisms to break several important symmetries are also included in the model. The broken symmetries are the invariances under charge conjugation, time reversal, and space inversion. Complete breaking of the charge conjugation and parity symmetries for the weak interaction are produced by the left-handedness of the W bosons.

The standard model also preserves the total number of quarks, as well as the number of particles of each lepton generation. This is represented by the conservation of the additive quantum numbers L_e, L_μ, L_τ, and B (electron, muon, tau lepton and baryon numbers). There is no conserved quark generation number. The total number of strange

and charm quarks (for instance) may be altered during a reaction or particle decay, unlike the total number of mu leptons and mu neutrinoes. The failure of quark generation conservation is assumed to be caused by the influence of the strong interaction, which mixes the weak interaction quark eigenstates. This is mathematically represented by

$$\begin{pmatrix} d' \\ s' \\ b' \end{pmatrix} = \mathbf{KM} \begin{pmatrix} d \\ s \\ b \end{pmatrix}. \qquad (1.1)$$

The d, s, and b represent the weak interaction eigenstates of the down, strange, and bottom quarks, while d', s', and b' are the physical (mass) eigenstates. **KM** is a 3 X 3 unitary mixing matrix call the "Kobayashi-Maskawa matrix" (Kob73). Thus the weak decay of a K^+ meson (a $u\bar{s}'$ quark combination) to π^0 (through $u\bar{u}$) e^+ ν_e is accomplished through the small admixture of d in s' due to the off diagonal element in **KM**. The **KM** matrix contains three independent mixing angles and one complex phase. The latter provides the mechanism for violating time reversal symmetry.

One consequence of the standard model of electroweak interactions is that the weak interaction can no longer be considered to be weak. The strength of an interaction is determined by the coupling constant, a dimensionless quantity which, along with statistical factors and interaction matrix elements, determines particle decay rates and reaction cross sections. The coupling constant of quantum electrodynamics is the elementary electric charge (e), the value of which is $e^2 = 1/137$ (in natural units, $c = \hbar = 1$). The coupling constant of the weak interaction is of the same order of magnitude, being $g \approx 0.1$. As will be explained in Section 3, the apparent 'weakness' of the weak interaction stems from the large mass of the W and Z bosons. For low energy processes - i.e. those in which the momentum transfer is small compared to the mass of the intermediate bosons - the effective coupling of the interaction is inversely proportional to the square of the boson mass. For

processes in which the momentum transfer is comparable to or greater than the W boson mass, the weak and electromagnetic coupling strengths are similar.

The standard model has withstood twenty years of experimental tests without significant revision and produced several impressive predictions, such as the existence and approximate masses of the W and Z bosons and the strength of the neutral current interaction. It however also contains several unpleasant features which doom it to remain a phenomenological theory. The model contains 21 free parameters, which is considered to be too many for a fundamental theory and suggest that the standard model is only a low-energy manifestation of the a more fundamental theory. There are also several assumptions built in, such as the number of particle generations and the exact equality of electron and proton electric charges, which should perhaps be explained on a more fundamental level. Many theories have been produced attempting to supercede the standard model and address some of these questions. Accompanying this theoretical effort is an experimental push to test the limits of the standard model. These investigations include searches for new particles, forbidden decays or reactions, and exotic interaction forms.

Section 1.3. Current-Current Interactions.

Although gauge theories such as the standard model are the most comprehensive representation of our knowledge of particle physics, for the purposes of discussing nuclear beta decay they are needlessly complicated. Assuming the mass of the gauge boson (83 GeV in the case of the W_L bosons) is much greater than the energy released during the decay (typically less than 10 MeV), an effective theory in which the bosons do not explicitly appear and their interactions are replaced by a local current-current interaction is adequate to describe all observables (Com83). In a theory of this type the fermion fields interact directly and all four fermions which participate in the decay are created or destroyed at the same point. This description contrasts with the standard model in which the two

quarks and the two leptons interact with the W boson field at different points (see Figure 1.1). The properties of the gauge boson field are absorbed into the coupling constants of the effective theory. The effective interaction which is traditionally employed to describe nuclear beta decay will now be examined.

The traditional interaction hamiltonian is constrained to be Lorentz invariant, local, and Hermitian. It must also conserve electric charge, nucleon number, and (perhaps) lepton number. To restrict the form of the interaction certain 'simplifying assumptions' are also adopted, which are that the hamiltonian depends only linearly on the fermion creation and annihilation operators and that no derivatives of these operators appear. The most general hamiltonian satisfying these conditions may contain only five terms which are labeled according to the transformation properties of the nucleon current under rotations and space inversion. These are the scalar, pseudoscalar, vector, axial vector, and (second rank) tensor interactions (Sch66).

The most general hamiltonian for an arbitrary interaction satisfying these constraints is

$$H_{INT} = \frac{G_F}{\sqrt{2}} \sum_i \left(\overline{\Psi}_e O_i \left(C_i + \gamma_5 C_i'\right) \Psi_\nu\right)\left(\overline{\Psi}_p O_i \Psi_n\right) + \text{h.c.} \qquad (1.2)$$

where

G_F = Fermi coupling constant,

Ψ = particle annihilation and creation operators,

i = S, V, T, A, P,

O_i = Dirac 4 x 4 matrix operators of type i,

γ_5 = Dirac parity operator,

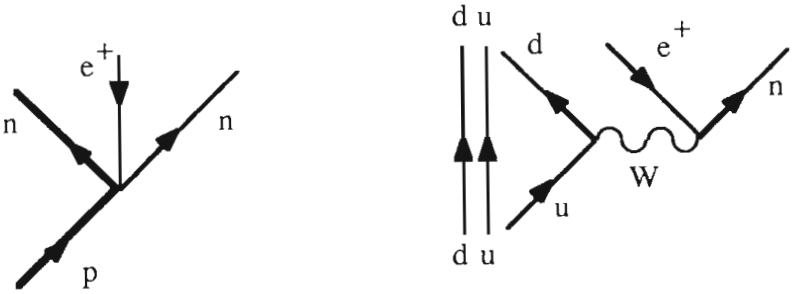

a) Positron Emission

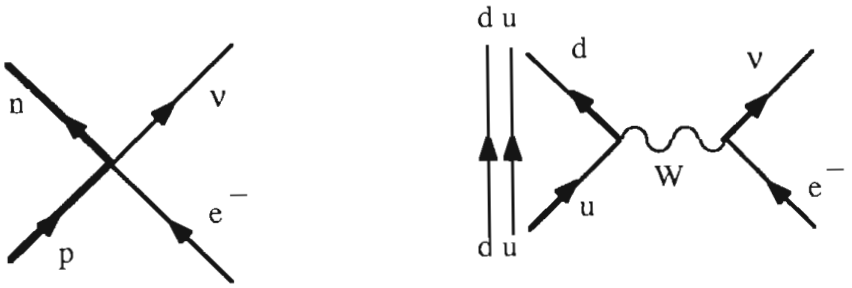

b) Electron Capture

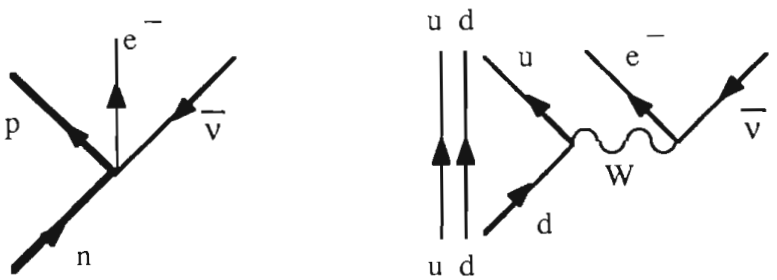

c) Electron Emission

Figure 1.1. Feynman diagrams for nuclear beta decay processes in both the effective theory and the standard model. In (a) and (b) a neutron is created and a proton is destroyed. In (c) a proton is created and a neutron is destroyed.

C_i = amplitude of interaction type i,

and $$\sum_i \left\{ |C_i|^2 + |C_i'|^2 \right\} = 1.$$

The structures $\overline{\Psi} O \Psi$ are the Lorentz invariant fermion currents which create and destroy particles at the point of interaction. The relative strengths of the various terms are given by the squares of the amplitudes C_i. The behavior of the interaction under the charge conjugation, parity, and time reversal transformations is determined by the values of the C_i and C_i'. If the amplitudes are all real (relative to a common phase) the interaction is invariant under time reversal. If the primed (or, equivalently, the unprimed) amplitudes are all zero the interaction conserves parity. The interaction is invariant under charge conjugation is the primed quantities are all real while the unprimed quantities are all imaginary (or vise versa).

The so-called Fermi coupling constant G_F determines the overall strength of the interaction which produces nuclear beta decay and is equal to 1.4×10^{-49} erg cm^3 (Sch66). Notice that this quantity is not dimensionless and therefore is not a true coupling constant. The relation between the Fermi coupling constant and the coupling constant (g) of the standard model is

$$\frac{G_F}{\sqrt{2}} = \frac{g^2}{8 M_W^2}. \qquad (1.3)$$

Prior to the development of the standard model, the weak coupling constant g was estimated using Equation 1.3 with the electron, pion, or proton mass in the place of M_W. This produced a quantity six to ten orders of magnitude smaller than g and caused the strength of the interaction to be greatly underestimated.

The hamiltonian of Equation 1.2 conserves lepton number. There continues to be speculation, but as yet no experimental evidence, that the neutrino and antineutrino are identical particles, $\nu = \overline{\nu}$. In this case a lepton number nonconserving hamiltonian must be added to H_{INT},

$$H_{NC} = \frac{G_F}{\sqrt{2}} \sum_i \left(\overline{\Psi}_e O_i \left(D_i + \gamma_5 D_i' \right) \overline{\Psi}_\nu \right) \left(\overline{\Psi}_p O_i \Psi_n \right) + \text{h.c.} \qquad (1.4)$$

This hamiltonian produces decays with $\Delta L = 2$, such as

$$n \rightarrow p + e^- + \nu \quad \text{or} \quad 2\,n \rightarrow 2\,p + 2\,e^-. \qquad (1.5)$$

The amplitudes C_i, C_i', D_i, and D_i' may be complex if time reversal invariance does not hold. Therefore these amplitudes (along with the normalization G_F) contain 40 real parameters. One is a common phase, which is of no physical consequence, leaving 39 parameters which must be determined to achieve a complete description of nuclear beta decay. The present limits on the values of these parameters will be discussed in Section 5.

The effective interaction hamiltonian corresponding to the familiar V-A form of the standard model is obtained by assuming (in the absence of strong interaction effects) $C_V = C_V' = -C_A = -C_A' = 1/2$ and setting all other coupling constants to zero. The evidence for the validity of the V-A form will be examined in Section 5.

Section 1.4. Nuclear Structure and Beta Decay.

Nuclear beta decay is the common name of several processes whereby neutrons are converted to protons, or vice versa, by emission or absorption of electrons, positrons, and neutrinos. These processes include:

electron emission	$n \rightarrow p + e^- + \overline{\nu}$	
positron emission	$p \rightarrow n + e^+ + \nu$	(1.6)

electron capture $p + e^- \rightarrow n + \nu$.

Feynman diagrams for these processes in both the standard model and the traditional effective theory are presented in Figure 1.1.

The previous sections have discussed the properties of the beta decay interaction hamiltonian. The properties of the nuclear levels linked by the transition however are determined by the strong and electromagnetic interactions. These levels affect beta decay rates and asymmetries through the nucleon current $\overline{\Psi}_p O \Psi_n$.

The initial and final states of the decaying nucleus are in general narrow and well separated from their neighboring states, thus the energy, spin, and (in some cases) isospin of the states linked by the transition are well-defined. The transition probability (w_{fi}) for the decay can be calculated using Fermi's Golden Rule No. 2 (Fer50),

$$w_{fi} = \frac{2\pi}{\hbar} \left| \mathcal{H}_{fi} \right|^2 \left. \frac{dn}{dW} \right|_0 . \qquad (1.7)$$

Here $\left. \frac{dn}{dW} \right|_0$ is the density of final states available to the system, which is completely determined by the distribution of the energy released to the leptons. $\mathcal{H}_{fi}$ is the matrix element of the interaction hamiltonian integrated over the nuclear volume and summed over all nucleons. Because the initial and final nuclear levels are well-defined, beta decay transitions are classified according to the properties of these states. The classification parameter is called the forbiddenness, with a larger forbiddenness corresponding to a smaller transition rate for decays with similar energy release.

Two effects contribute to the total forbiddenness of a transition. The first contribution is related to the orbital angular momentum carried off by the leptons. When the lepton wave functions are expressed as a multipole expansion, each succeeding term contains an additional factor of $\vec{k} \cdot \vec{R}$, where $\vec{R}$ is the coordinate of the point at which the

particle was created and $\vec{k}$ is the total linear momentum of the leptons. Since the hamiltonian represents a point interaction (see Section 3), $\vec{R}$ is confined to lie inside the nucleus, which has a radius of roughly five femtometers (0.004 / MeV in natural units). The energy released during the decay is typically 1 MeV to 10 MeV, therefore $\vec{k} \cdot \vec{R} \leq 0.1$. Each term in the transition matrix element therefore is roughly 10 times as large as the next, which results in each succeeding term's producing a transition rate which is smaller by a factor of 100 or more.

The second contribution to the forbiddenness of a transition originates with the nucleon current in the hamiltonian. For a non-relativistic or nearly non-relativistic fermion the upper two components of the Dirac spinor form a Pauli spinor normalized to one, while the lower two components form a Pauli spinor of opposite parity normalized to the particle velocity v/c (Sak67). These Pauli spinors are known as the large and small components of the wave function, respectively For nucleons bound in nuclei $v/c \approx 0.1$. If the nucleon current mixes the large and small components, the matrix element will be reduced by a factor of 10 and induce a parity change relative to an interaction which does not mix the components.

The total forbiddenness of a transition is defined as the combination of the forbiddeness arising from the nuclear angular momentum and parity changes. If $\vec{J}_L$ is the "orbital" angular momentum of the leptons, and P = 1 (0) if there is (not) a parity change caused by a mixing of the large and small components of the nucleon wave function, then the forbiddenness of a transition is $f = \vec{J}_L + P$. If $\vec{J}_i$ and $\vec{J}_f$ are the initial and final nuclear spin, the transition proceeds by all classes of forbiddenness which satisfy

$$| J_i - J_f | - 1 + P \leq f \leq J_i + J_f + P. \qquad (1.8)$$

Since an increase in f of 1 multiplies the transition rate by 0.01, the smallest value of f which satisfies the relations 1.8 dominates the transition. The diversity of the β-decay rates

in transitions with similar nuclear matrix elements and energy release is accounted for by the degree of forbiddenness of the transitions.

Transitions which have zero forbiddenness are traditionally said to be 'allowed'. An allowed transition is classified as being either Gamow-Teller (GT) or Fermi (F) depending on whether the spin of the decaying nucleon is flipped in the transition. The following selection rules for the change of the nuclear spin, isospin, and parity apply:

	$\Delta\vec{J}$	ΔT	$\Delta\pi$
Fermi	$\vec{0}$	0	No
Gamow-Teller	$\vec{1}$	0,1	No

Fermi transitions may be produced by scalar or vector interactions. Gamow-Teller transitions may proceed only via tensor or axial vector interactions.

The reduced half-life $t_{1/2}$ of an allowed transition can be calculated using Equation 1.6, with $t_{1/2} = (\ln 2) / w_{fi}$. It is usually written as

$$t_{1/2} \equiv \frac{T_{1/2}}{BR} = \frac{1}{f} \frac{K}{g_V^2 |M_F|^2 + g_A^2 |M_{GT}|^2} . \qquad (1.9a)$$

Here K is a constant,

$$K = (2 \pi^3 \ln 2 \hbar^7) / (m_e^5 c^4), \qquad (1.9b)$$

BR is the branching ratio of the transition, $T_{1/2}$ is the half-life of the parent state, and f is the statistical rate function, essentially the total number of states available to the two leptons. This is a function of the total decay energy and (because of the Coulomb interaction between the beta-particle and daughter atom) the atomic number of the nucleus. The M_F and M_{GT} are the Fermi and Gamow-Teller nuclear matrix elements appropriate for

the transition, and g_V and g_A are the effective vector and axial vector coupling constants. In the absense of strong interaction effects (see Section 2.4), the effective coupling constants are

$$g_i^2 = \frac{|C_i|^2 + |C'_i|^2}{M_W^2}, \qquad (1.10)$$

where M_W is the mass of the W boson (but see Section 2.4).

The allowed transitions are also divided into superallowed and allowed, unfavored classes according to the overlap of the initial and final nuclear wave functions. The initial and final states of superallowed decays have larger overlaps and transition matrix elements and therefore proceed at a greater rate than the allowed, unfavored decays. Transitions between isobaric analog states - states which differ only by replacement of a neutron by a proton or vice versa - are superallowed transitions and proceed predominately by Fermi decay.

Experiments on superallowed transitions are the simplest ones from which to draw inferences on the weak interaction. The operators for the allowed transitions, being of lowest order in the expansion of the particle wave functions, are simple compared to those for forbidden transitions. Furthermore, the nuclear matrix elements for transitions between analog or nearly analog states linked by the superallowed decay can in general be calculated with much greater accuracy than the matrix elements for transitions between non-analog states. Between states which are exact analogs the Fermi matrix element is the square root of a multiple of the neutron or proton excess. Therefore the uncertainties in nuclear matrix elements arising from nuclear structure are often much smaller for superallowed transitions than for other transitions.

Section 1.5. Experimental Limits on the Interaction Amplitudes.

Our understanding of the basic structure of the weak interaction was shaped by a series of experiments on nuclear beta emitters performed during the 1950's. After an initial period of confusion during which it appeared the weak force was composed of scalar and tensor terms (Rus53, Rus55), it was established that the interaction is composed primarily of vector (V) and axial vector (A) terms in the V-A form. A few of the more important early results are summarized here, followed by a description of the present situation.

A measurement of the beta-neutrino angular correlation in the decay of

$$^{35}\mathrm{Ar} \rightarrow {}^{35}\mathrm{Cl} + e^{+} + \gamma . \qquad (1.11)$$

(Her57) indicated that Fermi beta decay proceeded by a vector rather than a scalar interaction. Most of the strength (98%) of the decay is the predominantly Fermi transition between the ground states which are isobaric analogs. In this experiment the recoil spectrum of the daughter atoms was determined. As will be explained in Chapter 2 this spectrum is a function of the beta-neutrino angular correlation which, for a Fermi decay, is in turn a function of the relative strength of the vector and scalar interactions K_{SS}/K_{VV}, with K_{ij} defined by

$$K_{ij} = C_i^{*} C_j + C_i' C'^{*}_j . \qquad (1.12)$$

At roughly the same time the first evidence that parity is not conserved resulted from a measurement of the electron emission asymmetry from polarized ^{60}Co (Wu57). The asymmetry is the coefficient of a term in the decay probability proportional to $(\vec{p}_e \cdot \vec{J})$, where $\vec{p}_e$ is the electron momentum and $\vec{J}$ is the nuclear polarization. This is a pseudoscalar quantity, therefore this term violates space inversion invariance. The results of the measurement were consistent with maximal parity nonconservation.

Evidence that the Gamow-Teller transition results from an axial vector interaction was soon obtained by a measurement of the helicity of neutrinos emitted from ^{152m}Eu decay (Gol58). It was found that the neutrinos have negative helicity. Combining this with the decay asymmetry of positrons emitted from the Gamow-Teller decay of ^{60}Co (Wu57), it is possible to reach the conclusion that the interaction producing Gamow-Teller β^+ decay has axial vector rather than tensor symmetry. Diagrams showing the 'typical' decay pattern for axial vector and tensor interactions are shown in Figure 1.2.

The validity of the V-A form of the beta decay interaction was established by a measurement of the electron and antineutrino asymmetries in the decay of polarized neutrons (Bur60). This is the only mixed decay for which the Fermi and Gamow-Teller nuclear matrix elements, denoted by M_F and M_{GT} can be calculated easily and accurately, $|M_F^2| = 1$ and $|M_{GT}^2| = 3$. The asymmetries depend on the interference of the vector and axial vector interactions and therefore can be used to distinguish between V-A and V+A forms.

Since 1960 many experiments have been performed which provide information on the constants C_i and D_i of Equations 1.2 and 1.4. Paul used the accumulated data base to obtain best fit values for several of the constants simultaneously in 1970 (Pau70). To simplify matters he assumed the interaction conserved lepton number and was invariant under time reversal. He also only used data from allowed nuclear beta decays, which do not depend on the amplitudes C_p and C_p'.

Paul's data set consisted of a total of 70 measurements of the quantities listed in Table 1.1. He also listed, but did not use in his fits, data on electron-neutrino triple correlations from polarized nuclei and the half-life of the neutron. The data set included only measurements on transitions for which either no assumptions about nuclear structure needed to be made (pure Fermi or pure Gamow-Teller transitions and neutron decay), or

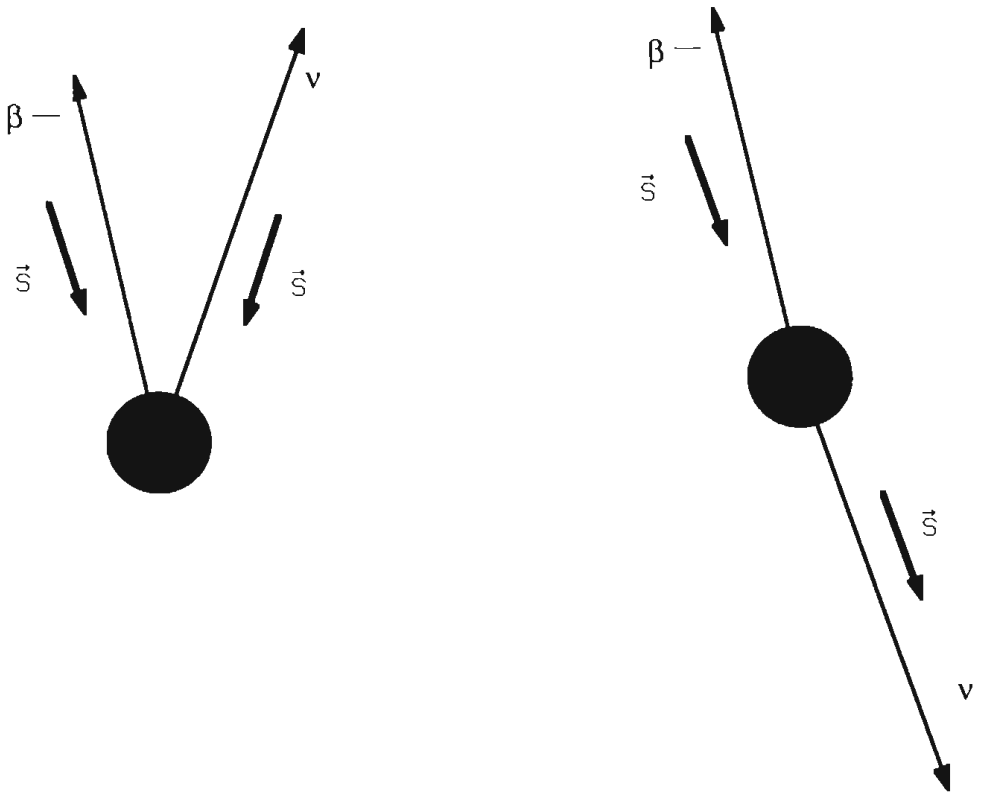

a) Tensor Interaction

b) Axial Vector Interaction

Figure 1.2. decay geometry for both the (a) axial vector and (b) tensor interactions. The direction of the spin of the leptons is indicated by $\vec{s}$. Note the change in the neutrino helicity.

Table 1.1 The quantities used in Paul's fit to the weak interaction transition amplitudes and the combinations of amplitudes constrained by each observable. $K_{ij} = C_i C_j^* + C_i' C_j'^*$ and $L_{ij} = C_i' C_j^* + C_i C_j'^*$. All observables except *a* and b have been multiplied by (1 + b / W), with W being the total energy of the beta-particle in units of electron rest mass.

Symbol	Measured Quantity	Transition Amplitudes
a	Beta-Neutrino Angular Correlation	$K_{TT} - K_{AA}$ and $K_{VV} - K_{SS}$
b	Fierz Interference Term	Re (K_{TA}) and Re (K_{SV})
A	Electron Asymmetry	$L_{TT} - L_{AA}$ and Re (L_{ST} - L_{VA})
B	Neutrino Asymmetry	$L_{TT} + L_{AA}$, Re (L_{TA}), Re($L_{ST} + L_{VA}$), and Re (L_{SA} - L_{VT})
Å	Electron-Circularly Polarized Gamma Angular Correlation	$L_{TT} - L_{AA}$ and L_{ST} - L_{VA}
G	Electron Helicity	$L_{TT} - L_{AA}$ and L_{SS} - L_{VV}

which could be assumed to proceed predominantly by the Fermi interaction (transitions between analog states in mirror nuclei and the decay of ^{14}O).

From the original 70 data values, a set of 12 measurements were selected and used to fit seven ratios of the amplitudes. The results were:

$$\frac{C_S}{C_V} = 0.08 \pm 1.2, \quad \frac{C_T}{C_A} = 0.006 \pm 0.2, \quad \frac{C'_V}{C_V} = 1.20 \pm 0.65, \quad \frac{C_A}{C_V} = -1.32 \pm 0.39,$$

$$\frac{C'_S}{C_V} = -0.07 \pm 1.0, \quad \frac{C'_T}{C_A} = -0.006 \pm 0.2, \quad \frac{C'_A}{C_A} = 1.11 \pm 0.07. \qquad (1.13)$$

The most recent comprehensive investigation of the relative magnitude of these amplitudes was performed by Boothroyd and others in 1984 (Boo84). Like Paul, they assumed that lepton number conservation and time reversal invariance holds and performed a fit to the ratios of coupling constants listed above. They determined that the V-A form explains all experimental results, but with rather large errors on a possible scalar interaction satisfying $C_S+C_S' = 0$. Their 95% confidence limits are

$$\left|\frac{C_S}{C_V}\right| < 0.23, \qquad \left|\frac{C_T}{C_A}\right| < 0.09, \qquad 0.65 < \frac{C'_V}{C_V} < 1.53,$$

$$\left|\frac{C'_S}{C_V}\right| < 0.19, \qquad \left|\frac{C'_T}{C_A}\right| < 0.085, \qquad 0.85 < \frac{C'_A}{C_A} < 1.18, \qquad (1.14)$$

$$\left|\frac{C_S + C'_S}{C_V}\right| < 0.065, \qquad \left|\frac{C_T + C'_T}{C_A}\right| < 0.01, \qquad -1.71 < \frac{C_A}{C_V} < -1.00,$$

The limit on C_S+C_S' is primarily a result of determinations of the shape of the Fermi transition beta particle energy spectrum (Thi78, Ram78), which depends on the Fierz

interference term. The limits on C_S and C_S' come from measurements of the neutron half-life (Chr72, Byr80, Bon78, Wil82) and beta-neutrino angular correlations (Rob58, Tre59, Gri68, Dob75).

Noting that the limits on C_S and C_S' are rather poor relative to the limits on the strength of the tensor interaction, we set out to improve the determination of these quantities. The method we chose is set forward in Chapter 2.

Chapter 2. The Beta-neutrino Angular Correlation Coefficient.

Section 2.1. Introduction.

The total scalar interaction strength $K_{SS} = C_S C_S^* + C_S' C_S'^*$ relative to the vector strength K_{VV} can be determined directly from a measurement of the beta-neutrino angular correlation for a Fermi transition. In the present work this correlation has been measured for the beta-delayed proton emitter ^{33}Ar. The background for this experiment will now be discussed.

We begin with a summary of beta-neutrino angular correlation measurements. The decay scheme of ^{33}Ar will be discussed next, followed by a description of the method we used to determine the correlation. The remainder of the chapter is dedicated to a discussion of the nuclear structure of ^{33}Cl, how the limits on our knowledge of the structure increase the uncertainty in the determination of K_{SS}/K_{VV}, and what information concerning ^{33}Cl can be extracted from our data.

Section 2.2. $\beta - \nu$ Correlation.

The beta-neutrino angular correlation is the probability that the two leptons created in beta decay are emitted in the same direction. It is parameterized by the correlation coefficient a in the relation

$$w\left(\theta, E_\beta\right) = \frac{1}{4\pi}\left(1 + a\,\frac{v}{c}\cos\theta\right), \qquad (2.1)$$

where θ = the angle between the directions of emission of the leptons,

v = electron velocity,

$w(\theta, E_\beta)$ = the probability per unit solid angle that the angle of emission is θ during a decay for which the positron has energy E_β.

Note that a is limited by $|a| < 1$. If $a > 0$ then the two leptons tend to be emitted in the

same direction. If $a < 0$ then they are more often emitted into different hemispheres.

The angular correlation coefficient is a function of the relative strengths of the terms in the weak interaction hamiltonian which produce the transition. Table 2.1 lists the value of the coefficient for transitions which proceed purely by each of the five interactions. The table also lists the lowest order nuclear beta decay which can be produced by each term.

Table 2.1. The beta neutrino angular correlation coefficient for the lowest order decay class produced by each of the five possible weak interaction terms.

Interaction	Angular Correlation Coefficient	Decay Class
Scalar	-1	Allowed Fermi
Vector	+1	Allowed Fermi
Tensor	+1/3	Allowed Gamow-Teller
Axial Vector	-1/3	Allowed Gamow-Teller
Pseudoscalar	-1	First Forbidden

Note that pure Fermi decay can be produced only by scalar and vector interactions, while only axial vector and tensor interactions can lead to Gamow-Teller transitions. The angular correlation coefficient for an arbitrary allowed decay is

$$a = \frac{\left(g_V^2 - g_S^2\right) B(F) + \frac{1}{3}\left(g_T^2 - g_A^2\right) B(GT)}{\left(g_V^2 + g_S^2\right) B(F) + \left(g_T^2 + g_A^2\right) B(GT)} \qquad (2.2)$$

where g_V, g_S, g_A and g_T are the effective vector, scalar, axial vector and tensor coupling constants discussed in Section 5. B(F) and B(GT) are the Fermi and Gamow-Teller transition strengths, the squares of the nuclear transition matrix elements. The transition strengths will be examined in Section 6.

As Equation 2.2 shows the angular correlation coefficient is sensitive to both the

relative strengths of the interaction terms and, through B(F) and B(GT), to the structure of the initial and final nuclear states. Historically measurements of a were employed first to establish the nature of the beta decay interaction and later for nuclear spectroscopy studies.

The angular correlation between two particles is most easily determined if both particles may be detected in coincidence with detector pairs placed at various relative angles. Since the neutrino is subject to only the weak interaction the neutrino detection efficiency of any detector is essentially zero and this 'direct' method cannot be applied. Determinations of the beta-neutrino angular correlation must therefore infer the direction of neutrino emission indirectly by measuring the momenta of the other two particles produced during the decay and employing conservation of momentum.

Although at first glance it would that appear the neutrino momentum could be determined by measuring the vector momenta of the beta particle and daughter atom for each event, only a few of the important angular correlation experiments have been performed this way. The reason is that the low recoil energy of the daughter atom, typically of the order of 100 eV, creates severe experimental difficulties. The cross section for scattering of these atoms is quite large, about 10^{-15} cm^2 (Rid61). As atomic scattering of course alters the momentum of the daughter atom, the source must be diffuse and the resulting signal to background ratios are small. Furthermore these low energy atoms are stopped in thin foils, so the source geometry cannot be arbitrarily limited in these experiments by thin walled gas cells or thin foil sources. The effective source volume must be determined from the geometry of the detectors and an integration over all possible angles of emission performed. For these reasons several workers in this field have noted that experiments which employed this method were prone to large systematic errors (Rid61, Vis63).

As stated above the early angular correlation measurements established the

dominant VA form of the weak interaction. The earliest of these experiments were determinations of a for the decay of ^{6}He, ^{19}Ne, ^{23}Ne, and ^{35}Ar (Her57 and All59). These measurements were performed by taking the recoil energy spectra of the daughter atoms without detecting the β-particle. Positive values of a - in which the leptons are usually emitted in the same direction - produce larger (average) recoil energies than negative values of a, therefore the shapes of the recoil spectra depend on the correlation coefficient. The results of these experiments were later confirmed for ^{6}He (Joh63) and ^{23}Na (Car63) using essentially the same method. Other determinations of correlation coefficients which produced evidence for the VA interaction include: a measurement of a for free neutron decay (Tre59), performed by detecting the proton and β-particle in coincidence; another experiment on free neutron decay in which the spectra of electrons were taken as a function of the electron-proton emission angle (Rob58); and measurements of a for ^{6}He (Rid61, Vis63), performed by measuring the spectrum of ^{6}Li recoil energies as a function of the β-particle energy.

Once the V–A form of the β-decay interaction was established the angular correlation was measured to determine the ratio between the axial vector and vector coupling constants g_{Afree}/g_V for free neutron decay (see Section 5). Notable experiments include a determination of a from the recoil spectrum of the protons (Dob75), and a measurement (Gri68) taken by detecting the proton and electron in coincidence.

Section 2.3. β - delayed Particle Emission and Decay of ^{33}Ar.

For the purpose of determining the scalar coupling strength we are interested in measuring the beta-neutrino angular correlation in the superallowed decay of ^{33}Ar to the analog state in ^{33}Cl, which has excitation energy of 5.546 MeV. The branching ratio is 30.7% (Bor 87). This state in ^{33}Cl then further decays by proton emission to the ground state of ^{32}S. Although proton decay to the first excited state of ^{32}S is energetically

permitted, this transition has not been observed. A simplified decay scheme for ^{33}Ar is presented in Figure 2.1.

Because protons emerge from a sample of ^{33}Ar whose mean lifetime is many orders of magnitude greater than that of the ^{33}Cl nuclei which decay by simple proton emission, this process is known as beta-delayed proton decay. For this decay scheme ^{33}Ar is called the parent or precursor, the daughter is ^{32}S, and ^{33}Cl is known as the emitter.

From the systematics of isotopic masses, it has been estimated that there is a total of about 1000 isotopes with observable delayed proton, neutron, or alpha-particle branches (Har74). Many examples of these decay modes have been identified, as well as several beta-delayed fission decays and the more exotic delayed two-proton decay (Ays85, Cab83, Hon83) and delayed triton emission (Bor86). There may also be delayed ^{3}He emitters (Har74).

Our interest in beta-delayed particle emitters stems from the fact that they provide a unique opportunity for studying beta-neutrino angular correlations. The emitted particles typically have energies of several MeV. They are therefore much easier to detect than the recoiling nucleus and can pass through thin foils without suffering large momentum changes. The lifetimes of the particle-unstable levels are usually shorter than 10^{-15} s, and therefore the particles are emitted before the emitter collides with neighboring atoms. The particles therefore retain information about the beta-neutrino angular correlation in their energy spectrum, as will be shown for the specific case of ^{33}Ar decaying to the analog state in ^{33}Cl.

In the superallowed decay of ^{33}Ar (see Figure 2.1), the ^{33}Cl atom acquires a recoil energy on the order of several hundred eV as a result of the beta decay. If the beta-neutrino angular correlation is positive - that is, if the leptons are usually emitted in the same

direction - this recoil energy is on average larger than if the correlation coefficient is negative. If only decays in which the β-particles have a specific momentum $p_\beta \hat{z}$ in the direction of the z -axis are selected, and the neutrino momentum is represented by

$$\vec{p}_\nu = p_\nu \left(\sin\theta \cos\phi \ \hat{x} + \sin\theta \sin\phi \ \hat{y} + \cos\theta \ \hat{z}\right) \tag{2.3}$$

where θ and ϕ are the polar and azimuthal angles of the neutrino momentum vector, then the average recoil momentum of the ^{33}Cl atom is given by

$$\overline{\vec{p}_{Cl}} = \iint -\left(\vec{p}_\beta + \vec{p}_\nu\right) w\left(\theta, E_\beta\right) d\Omega \tag{2.4}$$

Here $w(\theta, E_\beta)$ is given by Equation 2.1 and the magnitude of the neutrino momentum is determined by the conservation of energy to be the difference between the total decay energy and the total positron energy. The result of the integration of Equation 2.4 is

$$\overline{\vec{p}_{Cl}} = -\left(p_\beta + \frac{a}{3}\frac{v}{c} p_\nu\right) \hat{z} \tag{2.5}$$

Since the energy released in the decay of ^{33}Ar is 5 MeV and the mass of ^{33}Cl is roughly 30 GeV, Equation 2.5 gives less than 500 eV for the recoil energy of the ^{33}Cl atom.

A proton emitted in the direction $\hat{p}$ has a lab frame energy different than its energy in the ^{33}Cl rest frame because of the recoil velocity of the emitter. The energy of the proton in the lab frame is

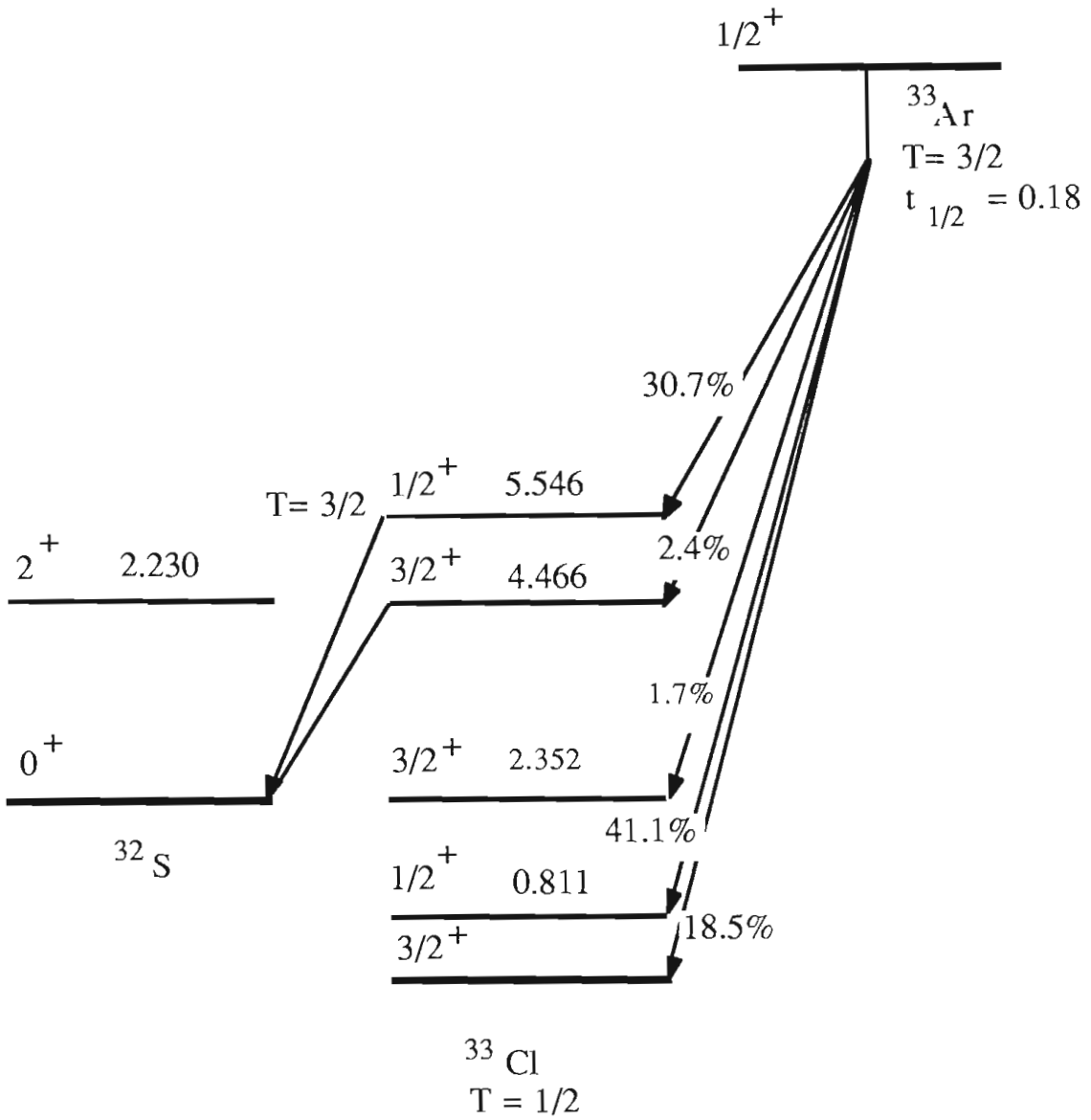

Figure 2.1. Simplified ^{33}Ar decay scheme. The energy released in the electron capture to the ^{33}Cl ground state is 11.6 MeV. The energy released in the proton emission in the decay from the analog state to the ^{32}S ground state is 3.2 MeV.

$$E_{\hat{p}} = \frac{1}{2} \frac{\left(\vec{p}' + \frac{m_p}{m_{Cl}} \vec{p}_{Cl}\right)^2}{m_p}$$
$$= E' + \frac{\vec{p}' \cdot \vec{p}_{Cl}}{m_{Cl}} + \frac{1}{2} \frac{m_p}{m_{Cl}^2} p_{Cl}^2 \qquad (2.6)$$

where the primed quantities refer to the proton momentum and energy in the rest frame of the emitter and m_{Cl} and m_p are the chlorine atomic and proton masses. The energy shift of the proton in the lab frame caused by the motion of the emitter is then

$$\Delta E_{\hat{p}} = E_{\hat{p}} - E'$$
$$= \frac{\vec{p}' \cdot \vec{p}_{Cl}}{m_{Cl}} + \frac{1}{2} \frac{m_p}{m_{Cl}^2} p_{Cl}^2 \qquad (2.7)$$

The protons are emitted in an $\ell = 0$ state ($\Delta J = 1/2$, $\Delta\pi$ = no for the nucleus) and their momentum is therefore not correlated with that of the leptons. The average energy shift for these protons is obtained by integrating the energy shift of Equation 2.7 over the correlation function given by Equation 2.1.

$$\overline{\Delta E_{\hat{p}}} = \iint \Delta E_{\hat{p}}\, w\left(\theta, E_\beta\right) d\Omega \qquad (2.8)$$

Selecting a reference frame in which the proton is emitted in the xz -plane with an angle α relative to the direction of emission of the beta particle (so $\hat{p} = \cos\alpha\, \hat{z} + \sin\alpha\, \hat{x}$), results in the following expression for the energy shift:

$$\overline{\Delta E_{\hat{p}}} = \frac{1}{2} \frac{m_p}{m_{Cl}^2} \left(p_\beta^2 + p_\nu^2 + a \frac{v}{c} \frac{2}{3} p_\beta p_\nu\right) - \frac{p' \cos\alpha}{m_{Cl}} \left(p_\beta + \frac{a}{3} \frac{v}{c} p_\nu\right) \qquad (2.9)$$

This is graphed for $a = 1$, 0 and -1 with $\cos\alpha = -1$ in Figure 2.2.

Our determination of the angular correlation takes advantage of the kinematics described above and consists of measuring the energy of protons emitted at $\pi/2$ and π from

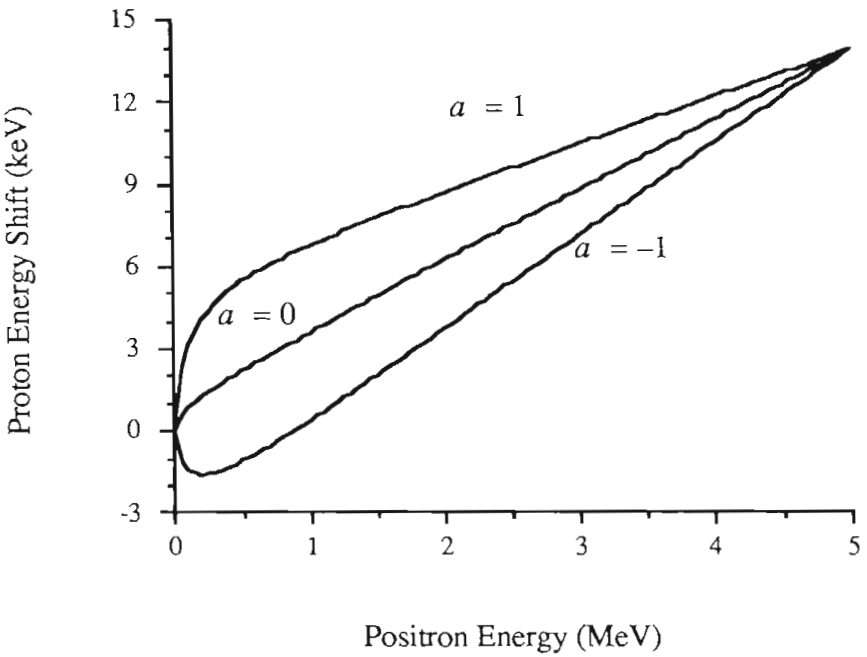

Figure 2.2. Proton energy shifts as a funtion of positron energy. The calculation is for decays in which the protons and positrons are emitted in opposite directions.

the direction of positron emission to find the energy shift as a function of beta-particle energy. The angular correlation coefficient a will be determined by fitting Equation 2.9 to the data.

Equation 2.9 may be applied to any beta-delayed particle emission for which either the beta-decay proceeds by pure Fermi decay, or the particle is emitted in an *s*-state relative to the daughter. The proton emitter ^{33}Ar was chosen because it satisfied the following conditions: light mass, relatively easy to produce, large energy release in both beta-decay and proton emission, well-defined analog state with a large branching ratio, and little Gamow-Teller strength relative to the Fermi strength. The last criteria is required so that contributions from the Gamow-Teller strength of the transition do not complicate the determination of the scalar-to-vector strength ratio. The other criteria were applied for experimental reasons. Notice that to first order the proton energy shift depends linearly on the momentum of the emitted particles and inversely on the mass of the emitter atom (see the second term on the right hand side of Equation 2.9), so that a light nuclear mass and large decay energies produce shifts which are large and hence easy to measure.

Equation 2.9 is not valid for those transitions which proceed by the Gamow-Teller interaction and are followed by p- or higher-wave angular momentum particle emission. In Gamow-Teller decay the leptons remove one unit of angular momentum from the nucleus. In this case, if only those transitions in which the beta-particles are emitted in a certain direction are selected (through detector placement), the emitter nucleus will in general be polarized along the axis of emission. The delayed particles will therefore not be emitted isotropically. To obtain the expression for the average energy shift of these particles the beta-neutrino angular correlation in the integrand of Equation 2.8 must be replaced by the triple correlation function of the three emitted particles, which depends on the sequence of nuclear spins. (The triple correlation coefficient for delayed alpha-particle emission has

been calculated in Hol74.)

Delayed proton emission has not been utilized previously to determine beta-neutrino angular correlations, but a few experiments on delayed alpha emitters have been performed using several different methods. The systems studied include ^{8}Li and ^{20}Na . The measurement of MacFarlane *et al.* (Mac71), determined the angular correlation coefficient from the analysis of the alpha-particle line shape (without taking beta-alpha coincidences). Clifford *et al.* (Cli89) and Barnes *et al.* (Bar58) measured kinematic energy shifts as a function of beta-particle energy using the method outlined above. Lauritsen *et al.* (Lau58) determined shifts indirectly by measuring the angle between the two beta-delayed alpha particles emitted in the decay of ^{8}Be.

Section 2.4. Effective Coupling Constants.

We now return to Equation 2.2 relating the correlation coefficient *a* to nuclear matrix elements and effective coupling constants. The values of both the matrix elements and the coupling constants depend on strong interaction effects and need to be discussed in greater detail. This section deals with the coupling constants. Nuclear matrix elements will be examined in Sections 5 and 6.

If nucleons were elementary particles the effective coupling constants would be identical to the constants of the underlying fundamental theory divided by the boson mass. Nucleons are complex objects, however, most likely containing three "valence" quarks and an "ocean" of virtual quarks exchanging real and virtual photons, W bosons, Z bosons, and gluons. The nucleon itself is surrounded by a cloud of virtual pions, electrons, and other particles. The electroweak fields interact with the virtual particles as well as the real ones. Therefore the nucleon current $\bar{\Psi}\gamma\Psi$ in the interaction hamiltonian (Equation 1.2), which represents a point particle, is not an accurate representation of the nucleon. A "correct" expression of the current, expressed as a sum over currents representing real and

virtual quarks, photons, antiquarks, etc., is beyond our present capabilities, and in any case would be so complicated as to prohibit calculations. Therefore a phenomenological adjustment is applied to the coupling constants in lieu of altering the expression for the currents. This process is known as "renormalization".

Because of renormalization there are several sets of weak interaction coupling constants between which we must differentiate. There are the coupling constant g of the standard model, the Fermi coupling constant G_F, and the constants g_V, g_A, g_S, and g_T of Equation 2.2. In addition, the amplitudes C_i of the effective hamiltonian of Equation 1.2 are usually also called coupling constants. Note that only g is technically a coupling constant in the language of gauge field theories. It describes the interactions of fundamental particles and its value is therefore derived from experimental data on the interactions of leptons, in particular from the muon decay rate. As mentioned in Chapter 1 it is of the same order of magnitude as the fine structure constant, $e^2 = 1/137$ (in natural units).

To determine the effective coupling constants we are faced with further complications. The hamiltonian of Equation 1.2 describes nuclear beta decay, with nucleons and leptons being treated as elementary particles. Nucleons however decay in nuclei which are complex objects, consisting of many nucleons exchanging real and virtual photons and mesons. We are therefore faced with another round of "renormalization", with the possibility that the "coupling constants" depend on the nuclear environment.

This situation is greatly simplified if we realize that the hamiltonian of quantum electrodynamics (QED) describes a vector interaction; the photon field is associated with currents of the form $\overline{\Psi}\gamma\Psi$. The strength of the interaction depends only on the electric charge of the particles, a strictly conserved quantity. Therefore the various currents $\overline{\Psi}\gamma\Psi$ of all the real and virtual particles in a complex object must "arrange" themselves to

preserve the overall strength of the interaction. The vector beta-decay interaction has the same form, $\overline{\Psi}\gamma\Psi$; therefore its "charge" g_V will also be "conserved" during renormalization. This argument is known as the Conserved Vector Current (CVC) hypothesis and was first advanced by R.P. Feynman and M. Gell-Mann (Fey58). The eventual development of the standard model, in which the vector weak interaction is closely associated with the electromagnetic interaction, made the CVC argument rigorous.

Assuming that there is no scalar contribution to the weak interaction, Fermi beta decay proceeds only by the vector interaction. Decay proceeding between two $J^\pi = 0^+$ states satisfies only the Fermi transition selection rules, and g_V can be determined from a measurement of the half-life, energy release, and branching ratio of the transition (Har74). In the context of the standard model, the interaction responsible for nuclear β-decay is identical to the one which causes muon decay:

$$\mu \rightarrow e^- + \overline{\nu_e} + \nu_\mu. \qquad (2.10)$$

This is the Universal Interaction hypothesis, which, combined with CVC, implies that the vector coupling constants for both processes are equal. CVC is therefore tested by comparing the coupling constants determined for allowed Fermi nuclear beta-decay to that derived for process (2.10). The nuclear transitions studied for this purpose are $J^\pi = 0^+$ to 0^+ decays between isobaric analog states, which have transition strengths B(F) = 2 (see Section 5).

Several corrections must be applied before the comparison between g_V and muon coupling constant (G_μ) can be made (Wil78). The first results from the deviation of the **KM** matrix (see Section 1.2 and Equation 1.1) from the unit matrix. Since the physical down quark d' is not identical to the weak interaction eigenstate d, so that $d' = (\cos\theta_c)\, d$, the nuclear beta-transition rate is reduced by a factor of $(1 / \cos\theta_c)^2$. (The mixing angle θ_c is traditionally called the Cabibo angle.) The second correction is applied to the nuclear

matrix element of the transitions studied. As will be explained in Section 5, this results in a reduction by the factor $(1-\varepsilon)$ from B(F) = 2. Finally, there are the "inner" (subnucleonic) and "outer" radiative corrections to the nuclear decay rate and a similar correction for the muon decay process. These are denoted by $\Delta_{\beta V}$, δ_c, and Δ_μ. With these corrections a "reduced" *ft*-value is calculated:

$$\mathcal{F}t = ft\left(1-\varepsilon\right)\left(1+\delta_c\right). \tag{2.11}$$

This is compared to an $\mathcal{F}t$-value derived from the unitarity of the **KM** matrix with coupling constants "corrected" using

$$\frac{g'_V}{G'_\mu} = \left(\cos\theta_c\right)^2\left(1+\Delta_{\beta V}-\Delta_\mu\right). \tag{2.12}$$

The result of this comparison confirms CVC (Wil78, Har90).

The coupling constants for the non-vector interactions do not enjoy a CVC type of immunity against renormalization. They are in general altered by both nucleonic and nuclear effects. These effects can produce interactions with symmetries unlike those of the fundamental interactions. This produces the so-called induced currents, which will not be discussed further here (see Sch66).

The effective axial vector coupling g_A has been found to depend on the mass of the relevant nucleus. To separate the nuclear effects from the nucleonic effects, the value of g_A for neutron decay is denoted g_{AFree} and derived from decay asymmetries and half-life measurements. As mentioned before this is a mixed Fermi and Gamow-Teller decay (with easily calculable transition strengths, B(F) = 1 and B(GT) = 3), so the value of g_{AFree} as a fraction of g_V can be extracted from, for instance, the beta-neutrino angular correlation, using the equation

$$\frac{g_{AFree}}{g_V} = \frac{|M_H|^2}{|M_{GT}|^2} \frac{(3-3\,a)}{(1+3\,a)}. \qquad (2.13)$$

The value of g_{AFree} is (Wil73):

$$\left| \frac{g_{Afree}}{g_V} \right| = 1.251 \pm 0.009. \qquad (2.14)$$

Extracting g_A for an arbitrary decaying nucleus is considerably more difficult because the transition strengths are in general difficult to calculate accurately. For low mass ($8 \leq A \leq 40$) isotopes the Gamow-Teller strengths may be calculated for all allowed decay branches using a global shell model (see Section 6). B(GT) also can be determined experimentally, via an accurate measurement of the decay branching ratios, half-life, and decay energy. The sum of the experimental and theoretical transition strengths are then compared, and the ratio is taken as g_A/g_{AFree}. This ratio is mass dependent (Bro85), with

$$\left| \frac{g_A}{g_{AFree}} \right| = 0.76 \pm 0.03 \qquad \text{for } A \approx 30. \qquad (2.15)$$

Hence $$\left| \frac{g_A}{g_V} \right| = 0.95 \pm 0.04. \qquad (2.16)$$

Section 2.5 Isospin.

The last topic which needs to be discussed is the nuclear transition strengths B(F) and B(GT) which are defined as the squares of the nuclear matrix elements. The topic of transition matrix elements is closely linked to isospin mixing, so a digression on the concept of isospin is necessary. Isospin (T) was invented to explain the similar masses of the neutron and proton and the rough equality of nn, np, and pp interactions. The neutron and proton are considered to be different states of a fundamental particle (the nucleon), which has spin 1/2 and isospin 1/2. The isospin operator obeys the same commutation relations as the angular momentum operator, hence the nucleon has two orthogonal states,

usually denoted by either isospin up and down or by $T_3 = +1/2$ and $T_3 = -1/2$. By convention the isospin up nucleon is the proton; the neutron has isospin down.

Just as the vector spins and orbital angular momenta of all the nucleons in the nucleus add to produce the total nuclear spin, the vector isospins of the nucleons add to yield a total nuclear isospin. The minimum isospin a nuclear state can have is one-half the neutron-proton excess. The ground states of nearly all isotopes have the minimum possible isospin (Tem74). Unlike angular momentum, isospin is not a strictly conserved quantity and T is not a good quantum number, particularly for heavy nuclei in which the isospin breaking Coulomb interaction is important.

With isospin defined, isobaric analog states can be introduced. Isobaric analogs are states in different isotopes of a mass chain which have identical structure, except that a neutron in one is replaced by a proton in the other. In other words they vary only in the value of T_3. Beta-decay transitions between exact analog states proceed predominately by the Fermi interaction and contain all the Fermi strength. Since isospin symmetry is broken, exact analog states do not in general exist. The Fermi transition strength to the analog state is therefore reduced as the analog state is fragmented among several nuclear levels. The Gamow-Teller strength between the (nearly) analog states may also be enhanced, except in the case of $J^\pi = 0^+$ to $J^\pi = 0^+$ transitions for which Gamow-Teller transitions are forbidden by the angular momentum selection rules.

The Fermi transition strength linking two states is found by taking the square of the matrix element of the Fermi operator $\sum_A t_\pm$, where $t_\pm$ are the isospin raising and lowering operators and the summation runs over all nucleons in the parent nucleus. If the initial and final states are represented by $|\,i\,\rangle$ and $|\,f\,\rangle$, the Fermi strength is

$$B(F) \equiv |M_F|^2 = \left| \langle f | \sum_A t_\pm | i \rangle \right|^2 . \qquad (2.17)$$

The Fermi operator connects only analog states, so both initial and final states have the same isospin T. If the third component of the isospin of the two states is denoted T_{3i} and T_{3f}, the Fermi strength between analog states can be written as

$$B(F) = [T(T+1) - T_{3i} T_{3f}] \delta_{fi} (1 - \varepsilon). \qquad (2.18)$$

The δ_{fi} expresses the fact that the transition proceeds between analog states, $(1 - \varepsilon)$ is a correction for the incomplete overlap of the parent and daughter wave functions caused by isospin mixing and charge dependent effects. Since the ground states of nuclei have the minimum possible isospin,

$$T_{zi} = (N - Z) / 2,$$

$$T = |T_{zi}|, \qquad (2.19)$$

and $$B(F) = 2T(1 - \varepsilon)$$

for decay between analogs.

The Gamow-Teller strength is found by substituting for the Fermi operator $\sum_A t_\pm \vec{\sigma}$, where $\vec{\sigma}$ is the spin operator. For a decay from a ground state, the <u>total</u> strength for electron emission and positron emission are denoted by $\sum_f B^-(GT)$ and $\sum_f B^+(GT)$, where the sums run over all possible final states whether the transition is energetically allowed or not. The Gamow-Teller strengths are related by the sum rule

$$\sum_A B^+(GT) - \sum_A B^-(GT) = 3(P - N), \qquad (2.20)$$

where P and N are the initial numbers of protons and neutrons.

For the superallowed decay of ^{33}Ar the Fermi transition strength can be estimated from systematics and the Gamow-Teller transition strength can be calculated using the shell model. From an analysis of the transition rates of 0^+ to 0^+ decays, Wilkinson (Wil73) determined the "mismatch" between analog levels for light nuclei reduces the Fermi transition strength by 0.3 ± 0.3 %. For ^{33}Ar this corresponds to $B(F) = 2.991 \pm 0.009$. The Gamow-Teller strength will be examined in the next section.

Section 2.6. The Nuclear Shell Model and GT Transition Strengths

Shell models are generated to reproduce the nuclear spectroscopy (level spins, parities, and binding energies) of a specified range of isotopes. The basis of a shell model consists of orbitals (single nucleon wavefunctions) of definite spin, isospin, and angular momentum. The hamiltonian of the nucleons in the shell is assumed to depend only on the occupation pattern of the orbitals. The effects of nuclear orbitals outside the model space and non-nucleonic degrees of freedom (such as the presence of delta isobars and pions) are ignored. The basis of shell models developed to date are limited to one major shell. Since highly excited nuclear states often contain nucleons promoted across shell boundaries such states cannot be described by these models. The useful excitation energy limit of an *sd*-shell model is roughly 6 MeV for nuclei in the middle of the shell (Wil84).

Modern calculations have been quite successful in the "*0p* shell" ($2 \le N, Z \le 8$) and the "*sd* shell" ($8 \le N, Z \le 20$). The *sd*-shell calculations are performed by assuming the first 8 neutrons and protons fill the (inert) ^{16}O core, with subsequent nucleons partially filling the $0d_{5/2}$, $1s_{1/2}$, and $0d_{3/2}$ orbitals. The shell model hamiltonian is assumed to be composed of two types of terms. The first type is the single particle level energy, which is essentially the binding energy of a nucleons in an orbital. The second type is the two-body

matrix element, which embodies the interactions of two nucleons in a given pair of orbitals. The coefficients of these terms are varied to reproduce the spectroscopy of the nuclei between ^{16}O and ^{40}Ca exclusive.

The shell model of Brown and Wildenthal (Bro85) fits the low-lying levels of 64 *sd*-shell isotopes to 150 keV rms deviation in the excitation energy of the levels. There are a few levels not explained by the model, most of which are states in nuclei close to the edge of the shell. These are "intruder" states, in which one or more nucleons is promoted either out of the ^{16}O core or into the *0f* (or a higher) orbital. The hamiltonian of this model has a mass dependence of $A^{0.35}$. The predecessor of the Brown and Wildenthal model, the Chung and Wildenthal model (Chu76) had no mass dependence but did not fit all isotopes in the shell with one hamiltonian. Two independent hamiltonians were produced for isotopes in the lower and upper halves of the sd-shell.

Once the shell model wave functions have been determined they can be used to calculate certain observables, such as nuclear magnetic moments, electromagnetic transition strengths, and Gamow-Teller decay strengths. This process consists of calculating the matrix elements of the appropriate operator between the states of interest. The choice of the operator is not a trivial matter, however. The model wave functions are not an exact representation of the nucleus (both because of the truncated basis of the model and the nonnucleonic degrees of freedom) and the normalization of the operator must be fit to the data. The observables listed above have been successfully studied in the context of the sd-shell model (Wil84). For Gamow-Teller transitions the renormalization of the operator results in $g_A = 0.76\ g_{Afree}$ as mentioned in Section 4. This renormalization is valid not only for beta decay, but also, to within experimental accuracy, for transition matrix elements obtained for (p,n) reactions at 100 to 200 MeV (Wil84). The (p,n) reaction also proceeds by the Gamow-Teller operator but samples a much larger region of excitation energy in the residual (daughter) nucleus than is possible with beta decay.

To estimate the Gamow-Teller transition strength we rely on two shell-model calculations. The first uses the wave functions of Brown and Wildenthal (Bro85) for the ground state of ^{33}Ar and its analog in ^{33}Cl. The second uses wave functions based on the Chung-Wildenthal interaction (Mul84). The two calculations produce B(GT) = 0.180 and 0.137, respectively, leading to

$$\frac{B(GT)}{B(F)} = 0.060 \text{ and } 0.046, \text{ respectively.} \qquad (2.21)$$

We will employ for this ratio the average of these two values, 0.053 ± 0.007.

Section 2.7. Summary

Assuming there is no tensor beta decay interaction, Equation 2.2 can be rewritten as

$$\frac{g_S^2}{g_V^2} = \frac{(1-a) + \frac{g_A^2}{g_V^2}\frac{B(GT)}{B(F)}\left(-a-\frac{1}{3}\right)}{1+a} . \qquad (2.22)$$

Employing the values for g_A/g_V (Section 4), B(GT) (Section 6), and B(F) (Section 5), we get

$$\frac{g_S^2}{g_V^2} = \frac{(1-a) - (0.048 \pm 0.011)\left(a+\frac{1}{3}\right)}{1+a} \qquad (2.23)$$

Note that the error caused by uncertainties of the nuclear structure do not exceed 1% for $a = 0.9$.

If for the moment we ignore the nuclear structure uncertainties and return to Equation 2.2 which expresses a as a function of the coupling constants and nuclear matrix elements, we find that a drops from $a = 0.939$ to $a = 0.851$ for values of $(g_S/g_V)^2$ of 0%

and 5%, respectively. Therefore to determine K_{SS}/K_{VV} to 2%, a must be measured to within roughly 0.035.

Alternatively, Equation 2.2 can be solved for B(GT)/B(F) as a function of a assuming $g_S = 0$:

$$\frac{B(GT)}{B(F)} = \frac{g_A^2}{g_V^2}\frac{(1-a)}{\left(a+\frac{1}{3}\right)} \tag{2.24}$$

Information about isospin mixing in ^{33}Cl can then be extracted from the correlation coefficient by comparing the experimental and theoretical (shell model) values of B(GT).

The details of the experiment which measured a for the superallowed decay of ^{33}Ar are presented in Chapter 3. In Chapter 4 the results of the analysis of the experimental data in terms of Equations (2.22) and (2.23) are reported.

Chapter 3. Experimental Equipment and Procedures.

Section 3.1. Introduction.

In Chapters 1 and 2 the importance of the beta-neutrino angular correlation was established. In the present chapter the experimental equipment and procedures which we used to measure the angular correlation coefficient in ^{33}Ar decay are reported. Section 2 contains the description of the equipment used to obtain a sample of ^{33}Ar in our counting chamber. Section 3 provides the details on the detectors and their associated electronics. The calibration of the detectors is described in Section 4. In Chapter 4 the method utilized to analyze the data is outlined.

Section 3.2. ^{33}Ar Production and Transport.

The first obstacle to the study of ^{33}Ar is obtaining a sample of sufficient activity in a volume with low background. Because of the short (175 ms) half-life of the isotope, ^{33}Ar must be produced on site through a nuclear reaction. Observing this decay in-beam is extremely difficult, however, because the radiation associated with the beam produces high levels of background in any detectors placed close enough to the production target to obtain a useable count rate. To avoid this radiation ^{33}Ar was transported away from the production target to a relatively low-background counting chamber.

The method and apparatus employed in the production and transport of ^{33}Ar in this experiment was similar to that used by Esterl *et al.* (Est71) in the pioneering studies of the decay of this isotope. Figure 3.1 contains a schematic of the equipment. ^{33}Ar was produced via the ^{32}S(^{3}He,2n) reaction by bombarding CS_2 gas with 700 nA of 24.2 MeV ^{3}He^{++} beam from the FN tandem Van de Graaff accelerator at Triangle Universities

Figure 3.1a). The ^{33}Ar production and transport system. ^{33}Ar was produced in the target by ^{3}He bombardment of ^{32}S and pushed to the counting chamber by a puff of helium gas. The flow of gases was determined by the computer-controlled solenoid valves shown in the figure. The number by each valve refers to the time line of Figure 3.1b, which shows the state of each valve during a production cycle ("High" means the valve is open, "Low" signifies closed). The total time for each cycle was about 1.5 s. Manually operated valves are not shown in the figure.

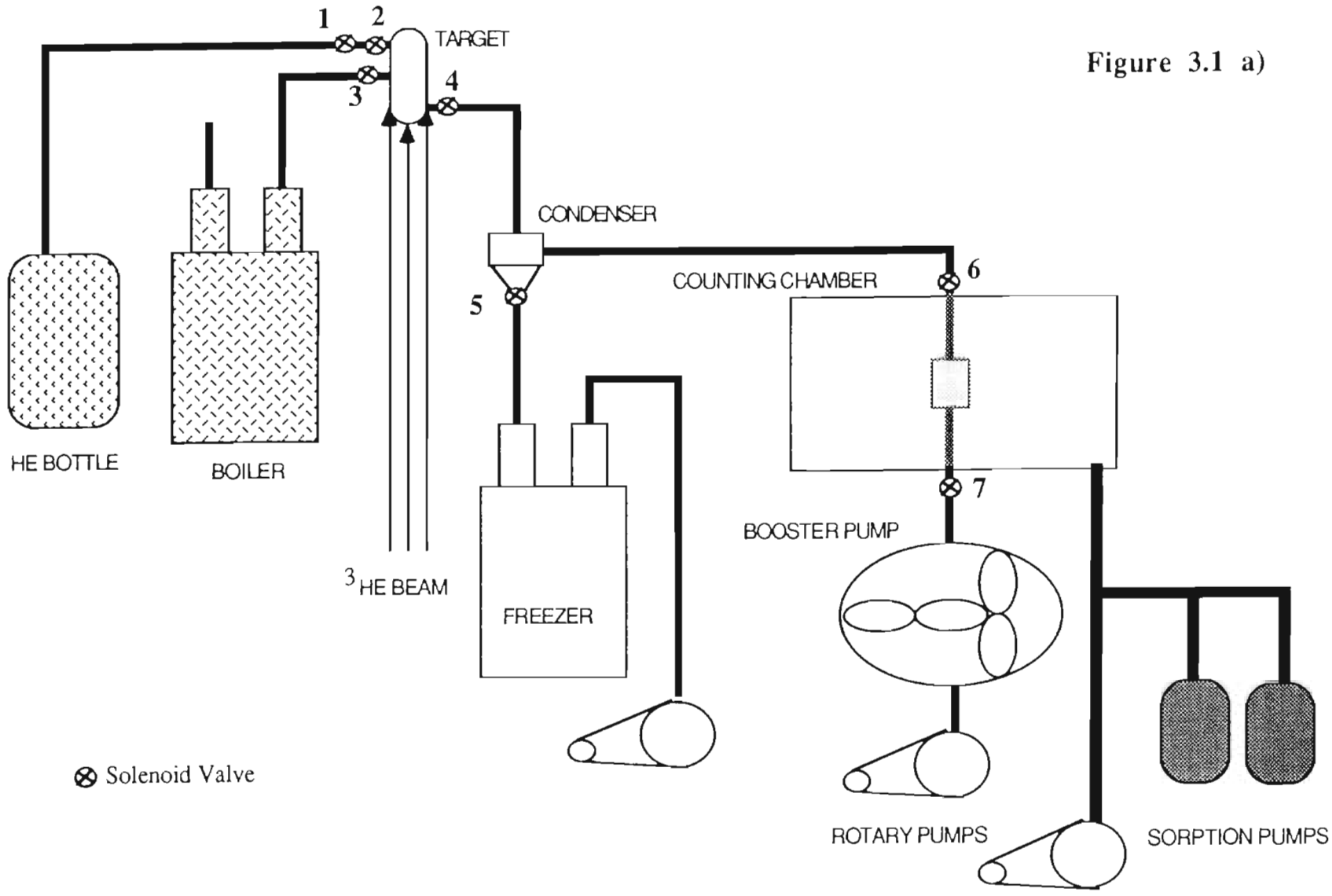
1
2
TARGET
3
4
CONDENSER
5
COUNTING CHAMBER
6
HE BOTTLE
BOILER
^{3}HE BEAM
FREEZER
7
BOOSTER PUMP
ROTARY PUMPS
SORPTION PUMPS
⊗ Solenoid Valve

Figure 3.1 a)

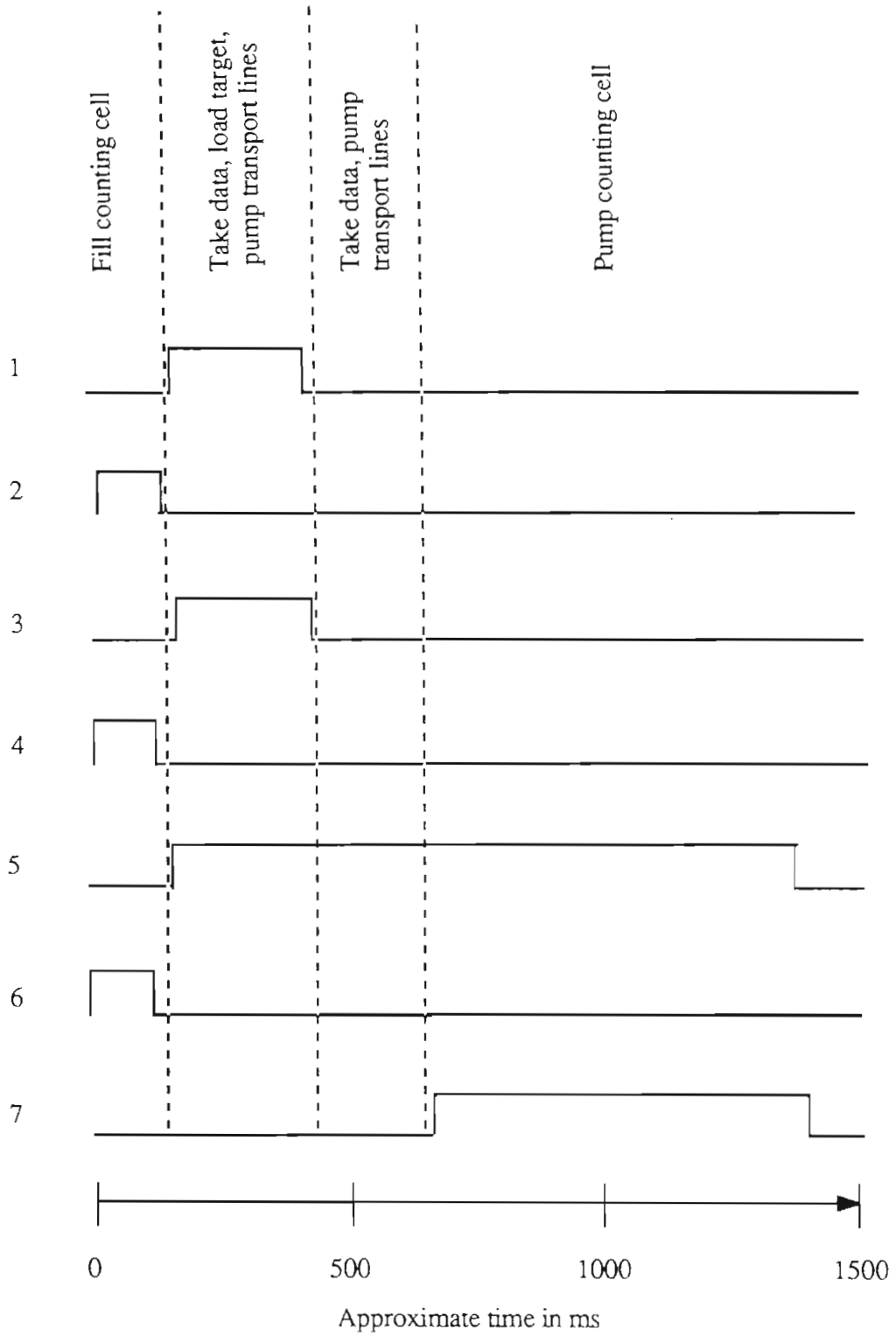
Fill counting cell
Take data, load target, pump transport lines
Take data, pump transport lines
Pump counting cell
1
2
3
4
5
6
7
0
500
1000
1500
Approximate time in ms

Figure 3.1b)

Nuclear Laboratory (TUNL). The target gas was then pushed through a dry ice trap, which liquified much of the CS_2, to the counting chamber by a puff of ^4He. Data were collected for several half-lives, then the counting cell and gas lines were pumped out. In the meantime more ^{33}Ar was produced in the target and another load of ^4He carrier gas was prepared. The movement of the gases was determined by a series of computer-controlled solenoid valves. The time structure was optimized to provide the highest yield of ^{33}Ar in the counting chamber. A time line is included in part b) of Figure 3.1 which indicates the state of each valve over the course of a production cycle.

In addition to initiating nuclear reactions in the target, the ^3He beam dissociated CS_2 molecules, producing a fine dust of sulfur and carbon in great quantities. This dust, unpleasantly radioactive, clogged the transport system's lines, valves, and cavities, thus creating a need for frequent maintenance. Most critical elements of the equipment were duplicated (or triplicated) and designed to be quickly replaced to minimize downtime and limit the exposure of personnel to the radiation emanating from the target. Despite these efforts, the effective data collection time was only about 50% of the real time, in part because the target was allowed to 'cool' 30 minutes before it was maintained. Radiation levels within a few cm of the target were then a few times 10 mrem/hr.

The production targets were three identical 10 cm long by 5 cm diameter aluminum cylinders with a 0.95 cm diameter hole body drilled along the axis. The vapor pressure of CS_2 during bombardment was approximately 1/3 atmosphere, presenting a target with total mass thickness of about 25 mg/cm^2 to the beam. The front apertures were covered by 6.25 μm havar foil through which the ^3He beam passed. The rear apertures were covered by 3 mm aluminum plates which were insulated from the bodies of the targets and used as unsuppressed Faraday cups for beam tuning purposes. Each target was removed after 12 hours in beam and placed in a lead house for at least 15 hours to allow beam-induced

radioactivity to die down. The cooled targets were then cleaned and rebuilt with the front foil and rear plate's being replaced. If the targets were not removed from service after a half-day's exposure to beam, the front foils ruptured. These failures were presumably caused by a combination of fatigue under the stress of repeated pressure changes in the cell, radiation damage, and the effects from the layer of sulfur dust which collected on the foil. This sulfur layer increased both the mechanical and, by absorbing beam energy, thermal stresses on the foil.

The gas lines between the target and counting cell were 6 mm inner diameter copper tubing. The dry ice trap was a 3.8 cm diameter by 0.95 cm deep cavity in a brass block partially submerged in a dry ice-ethanol mixture (T = 196K). A valve at the bottom of the trap allowed liquified CS_2 to drip out of the trap during pump out. The target-to-trap and trap-to-counting chamber lines were each approximately 80 cm long.

The efficiency of the transport system plummeted if the residual pressure in the gas lines increased above a few Torr at the start of the helium sweep. Therefore several cm^3-atm. of gas at pressures of several Torr had to be evacuated every second, with large periodic fluctuations in the input pressure. The pumping system built to achieve this contained three major elements. The first was a liquid nitrogen cold trap, which froze out the CS_2 gas. The other two elements were a Roots-blower-type booster pump backed by a conventional mechanical rotary pump, which removed the helium carrier gas and any air that entered the system through leaks or routine maintenance. The diameter of the lines connecting the pumping and transport systems were as large as conveniently possible, which both minimized the flow resistance and, by creating a reservoir with a large volume, reduced the pressure fluctuations inflicted upon the pumps.

Section 3.3. Detector Geometry and Detection Electronics.

In Section 2.5 the average energy of the protons emitted from a sample of ^{33}Ar was derived as a function of the beta-neutrino angular correlation coefficient, the energy of the positron, and the relative positron-proton emission angle. The average energy was shifted up to 14 keV relative to the energy of the protons in the ^{33}Cl rest frame. The angular correlation could in principle be determined by measuring the absolute energies of the protons detected in coincidence with positrons, but this would require detailed knowledge of both the response of the detection system and all the energy losses suffered by the protons in flight. A more accurate procedure was required. The method used was to measure only the relative energy shifts of protons observed in one detector coincident with positrons detected in two counters placed at different angles relative to the proton detector. Since the proton energy loss mechanisms are similar for both types of coincidences, only knowledge of the detector gain in the energy region around the emission line and corrections for the differing detection geometries is required. Our determination of the correlation coefficient consisted of taking the spectra of protons emitted at 90° (no proton energy shift) and 180° (maximum proton energy shift) relative to the direction of emission of positrons for various positron energies. The energy shifts (the difference between the centroids of the peaks in the two sets of spectra) were then compared with shifts calculated using Equation 2.9 for various values of a with appropriate corrections applied for the experimental geometry.

Figure 3.2 is a schematic of the contents of the counting chamber. The counting cell was a right parallelepiped with sides of 16 mm by 16 mm by 20 mm. The cell was milled from a solid block of aluminum leaving 1.6 mm thick posts at the four corners. The four "horizontal" side walls of the cell were made of 6 μm thick aluminized mylar foil. The cell was observed by four detector telescopes arranged every 90° around the cell on the

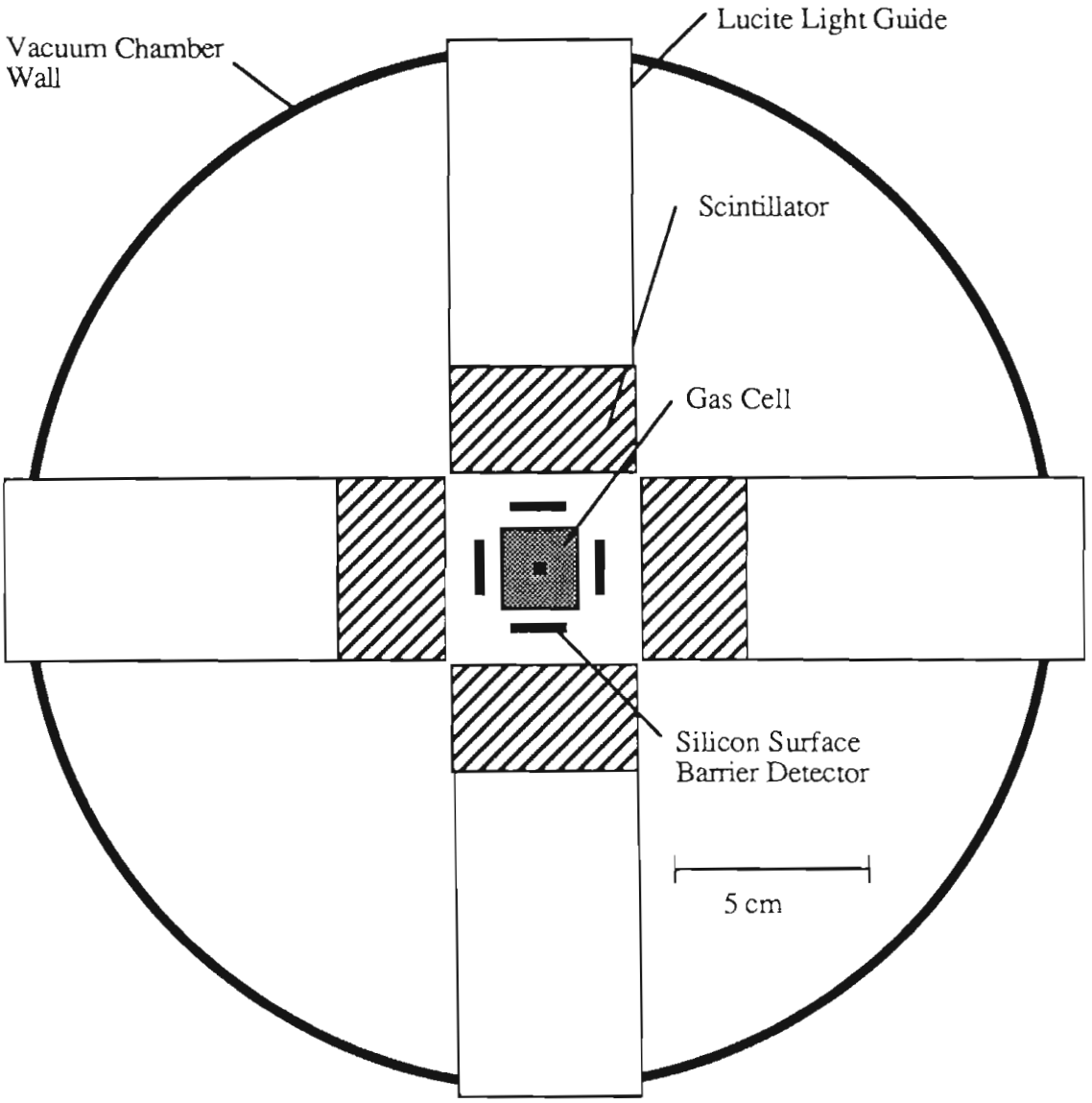

Figure 3.2. The counting chamber setup. The silicon detectors were 300 μm thick 150 mm^2 area transmission surface barrier detectors. The scintillators were composed of 5.1 cm diameter, 3 cm thick NE 102 plastic. The gas cell walls were 6 μm aluminized mylar foil. The light guides extend several inches beyond the vacuum chamber wall and are coupled to RCA 8575 photomultiplier tubes.

horizontal plane. Each telescope consisted of a high quality transmission-type silicon surface barrier detector with a surface area of 150 mm^2 and a thickness of 300 μm backed by a 5.1 cm diameter by 3.2 cm thick cylindrical plastic scintillator. The scintillator was connected via a 13 cm long by 5.1 cm diameter cylindrical Lucite light pipe to an RCA 8575 phototube biased between 1500 and 1600 V. The silicon detectors were chosen to be thick enough to absorb ~ 100 keV when a positron with an energy of 1 to 5 MeV passed through. This was adequate to separate positron signals from the noise of the detectors, which was less than 35 keV. This thickness of silicon is also sufficient to stop all proton groups emitted in the decay of ^{33}Ar.

The detectors, detection electronics, and data acquisition procedures were designed to select from all other signals events in which the proton and positron were observed in two different detector telescopes. The other types of events present included: protons detected without a corresponding beta-particle signal ("singles protons"); beta particles from both ^{33}Ar and other radioactive isotopes detected without a coincident proton; gamma rays from nuclear de-excitation of the decay products of ^{33}Ar and other radioactive isotopes, mainly ^{33}Cl and ^{34}Cl; and 511 keV positron-annihilation photons. A valid proton beta-particle coincidence event from the superallowed decay branch produced a signal in three detectors: a 3.1 MeV pulse in the silicon detector in which the proton was stopped, a low energy (about 100 keV) pulse in the silicon detector which was in the path of the positron, and a signal in the scintillator of the same telescope corresponding to the remainder of the electron energy. The use of both elements of the telescopes to detect the positrons was of vital importance. The silicon detector both improved the beta detection geometry and, by providing a veto against any photons which deposit energy in the scintillators, eliminated most of the background events.

The electronics which analyzed the pulses from the detector is shown schematically in Figure 3.3. The system was designed to collect all events in which a signal in any one of the silicon detectors exceeded a level corresponding to an energy of about 1500 keV, regardless of whether a valid beta particle signal was present. In brief, the electronics operated as follows. When a silicon detector produced a signal (which will be called the proton signal) of sufficient amplitude, an event gate was generated and each of four time to analog converters (TACs) was activated. The proton signal was shaped in a linear amplifier and presented to a Northern Scientific peak sensing analog-to-digital converter (ADC) for energy analysis simultaneously with a digital routing pulse which encoded the information about which detector initiated the event. The conversion gain of each ADC corresponded to roughly 1 keV/channel. Simultaneously, an independent circuit tested for signals coincident within 100 ns between the silicon and scintillation detectors in each telescope. If the coincidence requirement was satisfied, a stop signal was sent to the TAC corresponding to that telescope, an analog signal containing the telescope routing information was generated, and the scintillator energy signal was presented to a LeCroy 12 input current integrating ADC (model 2259A). The TAC signals were also sent to a LeCroy ADC. The conversion gain in the ADCs digitizing the positron energy signal corresponded to about 10 keV/channel, while that of each TAC ADC was about 10 ns/channel. Both LeCroy ADC's were activated by the event signal derived from the logical OR of the proton routers of the four silicon detectors.

The electronics therefore presented 14 digitized signals to the computer interface for each event: four proton energy signals (only one of which was valid), four scintillator energy signals (again, only one was valid), 4 time to analog converter (TAC) signals (one for each telescope), the telescope router signal, and the proton router. This information was stored on tape in 13 two-byte words.

Figure 3.3. Schematic of the detection electronics. Except for the modules in the dashed boxes, all of the electronics was replicated three additional times to process signals from telescopes 2, 3, and 4. The connection of the replications to the 'common' equipment in the dashed boxed is indicated by the heavy lines. Electronics for scalars and some delay lines are not shown.

The key to the diagram is:

ADC	Analog to Digital Converter
CFD	Constant Fraction Discriminator
G&D	Gate and Delay
LGS	Linear Gated Stretcher
SSB	Silicon Surface Barrier Detector
S&I	Sum and Invert
TAC	Time to Analog Converter
TFA	Timing Filter Amplifier

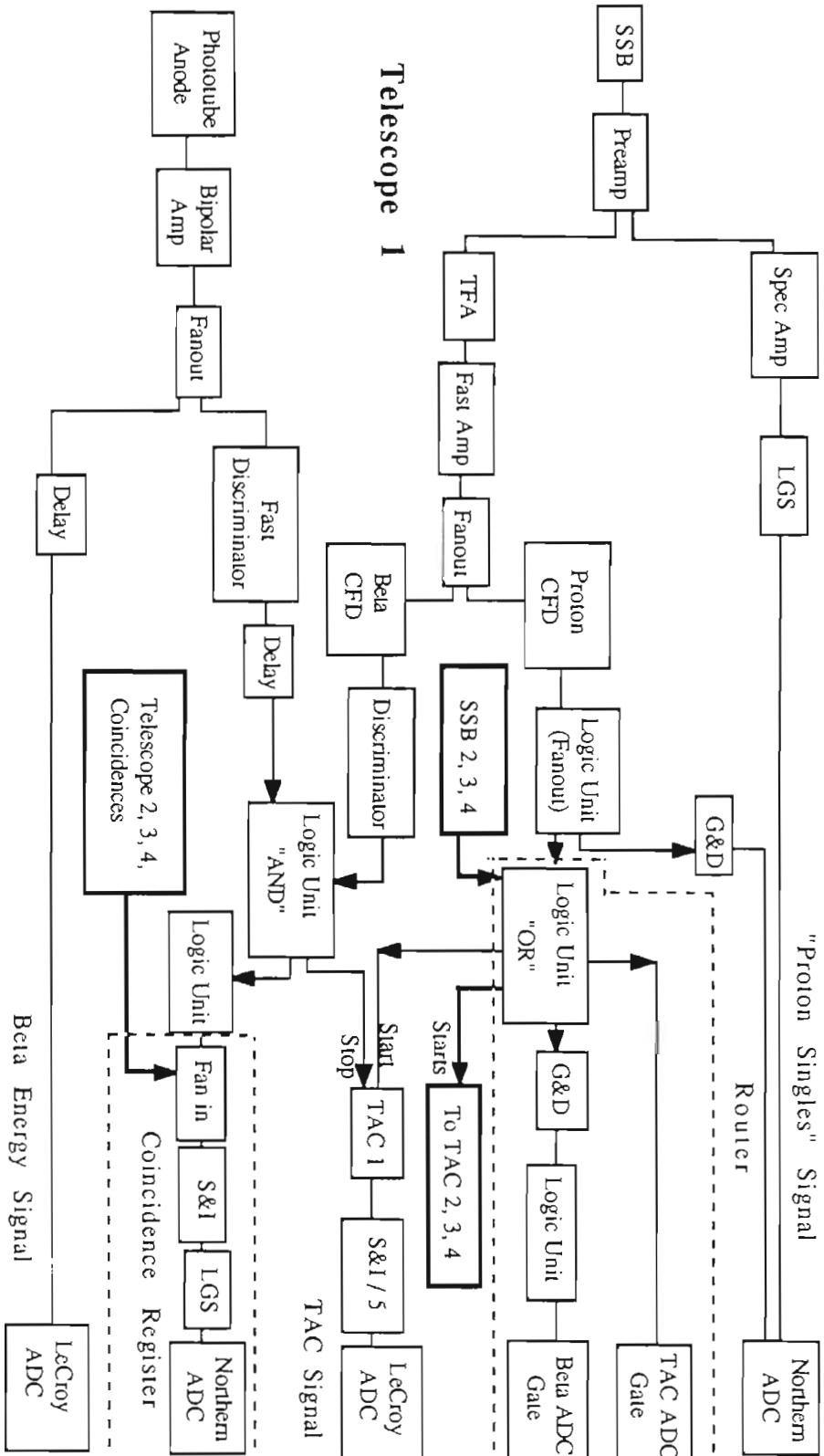
Telescope 1
SSB
Preamp
Spec Amp
LGS
"Proton Singles" Signal
TFA
Fast Amp
Fanout
Proton CFD
Logic Unit (Fanout)
G&D
Router
Northern ADC
TAC ADC Gate
Beta ADC Gate
Logic Unit "OR"
G&D
Logic Unit
Beta CFD
Discriminator
SSB 2, 3, 4
Starts
To TAC 2, 3, 4
Start
Stop
TAC 1
S&I / 5
LeCroy ADC
TAC Signal
Phototube Anode
Bipolar Amp
Fanout
Delay
Fast Discriminator
Delay
Logic Unit "AND"
Telescope 2, 3, 4, Coincidences
Logic Unit
Fan in
S&I
LGS
Northern ADC
Coincidence Register
Beta Energy Signal
LeCroy ADC

The TUNL data acquisition system consists of a microprocessor controlled CAMAC based interface and a Digital Equipment Corporation VAX 11/780 computer. When any detector produced a proton signal, the detector signals were processed as described above. When the ADCs completed digitizing all of the signals, the interface transferred the data into a buffer in VAX memory and reset the electronics in preparation for the next event.

The data were handled using the XSYS EVent Analysis Language (EVAL) (XSYS87). The data from all events with a proton signal corresponding to an energy of about 1800 keV or greater were stored on magnetic tape for later analysis. The threshold of 1800 keV was chosen because the background rose sharply below this energy; a lower cutoff resulted in an unacceptable increase in the number of uninteresting events being stored. On-line sorting of the proton signal was performed using the proton routers, telescope number signal, and TAC signals to allow the experimenters to monitor the data collection. The parameters monitored were the proton singles signals, coincidence register, protons signals in coincidence with each of the beta telescopes, the TAC for each telescope pair, and the scintillator energy signal in coincidence with each surface barrier detector.

One potential flaw with this data acquisition system stems from the specific features of the design of the TUNL computer interface. In TUNL's data acquisition system the Look-At-Me (LAM) signal from each CAMAC slot, which indicates that the module in that slot requires attention (usually by reading data out to the crate controller), are routed to a locally designed "LAM Panel". The LAM Panel allows the experimenter to define an event as being a combination of modules by merely pushing a selected set of buttons. If the experimenter defines an event to be composed of, for instance, data from ADCs in slots 2 and 3, the interface will take no action until both ADC 2 and ADC 3 produce a LAM. If

ADC 2 digitizes a signal but ADC 3 fails to produce a LAM for any reason, the interface will take no action and ADC 2 will hold its data indefinitely.

A problem arises with the TUNL implementation if, as in our case, an event is defined to consist of data from both Northern and LeCroy ADCs. (Use of Northern ADCs for proton energy measurements was necessary because the LeCroy ADCs do not have sufficient resolution.) The LeCroy ADCs are CAMAC modules which take on the order of 100 μs to digitize an incoming signal. The Northern ADCs however are not CAMAC modules. When they have completed digitizing, their output is sent to CAMAC input registers. When all modules associated with an event have raised a LAM the Northern ADCs are reset and are ready to accept the next input, regardless of whether any other modules (in particular the LeCroy ADCs) have been reset. Therefore a window corresponding to the time required to read and reset the LeCroy ADCs (about 50 μs) exists during which the Northerns will accept data and the LeCroys will not. If an event arrives during this time, the Northern ADCs will digitize and hold their data until the LeCroy ADCs accept and digitize data from the next event to arrive. The data which reaches the computer is then a mixture of two events.

To avoid collecting "mixed" events, the data rate was kept to a few hundred Hz through the proton energy signal discriminator. The fraction of data which is contaminated by these "mixed events" was monitored by looking at the fraction of high energy beta-particle signals (which are digitized by a LeCroy ADC) stored for correct and incorrect telescope number signals (which were digitized in a Northern ADC). This fraction is roughly equal to the ratio of mixed-to-unmixed events. The rate of mixed events was found to be negligible.

Section 3.4 Detector Calibration.

We now turn to the determination of detector calibrations. The silicon detector calibrations are established by using the most prominent peaks in the delayed proton spectra. Determining the response of the telescopes to positrons is a greater challenge because of the absence of a monoenergetic source of positrons and the complicated response function of the scintillation detectors.

The silicon detector energy calibrations were calculated from the position of the proton singles peak for four prominent ^{33}Ar decay branches (see Figures 2.1 and 3.4). The proton energies of these peaks were taken from [Bor87], with a correction for the energy lost in the cell wall.

Rather than attempting to measure the physical thickness of the foil and calculating the appropriate energy loss, we determined directly the proton energy loss in the foil in a seperate experiment. Protons from the TUNL van de Graaff accelerator were scattered from a thin natural carbon foil and detected with a 300 thick μm surface barrier detector at a scattering angle of 50°. The detector was calibrated by varying the lab-frame energy of the incident proton beam from 3.100 to 3.700 MeV in 100 keV steps. The beam energy was derived from a calibrated NMR signal of a bending magnet. The centroids of the collected spectra were taken and the conversion gain of the detection system calculated. The beam energy was then set to 3.400 MeV (the energy of those protons scattered at 50° then had an energy of 3.201 MeV) and two samples of the mylar foil were sequentially placed between the carbon foil and detector (see Figure 3.5). The energy loss of the protons in the mylar was then determined directly from the position of the resulting peaks (Figure 3.6). This energy loss was found to be 82.6 ± 1.0 keV for 3.2 MeV protons. The physical thickness of the foil was then determined using the energy loss program BABEL (Iko73, Iko75). BABEL divides the foil into regions of small energy loss and calculates the average loss in

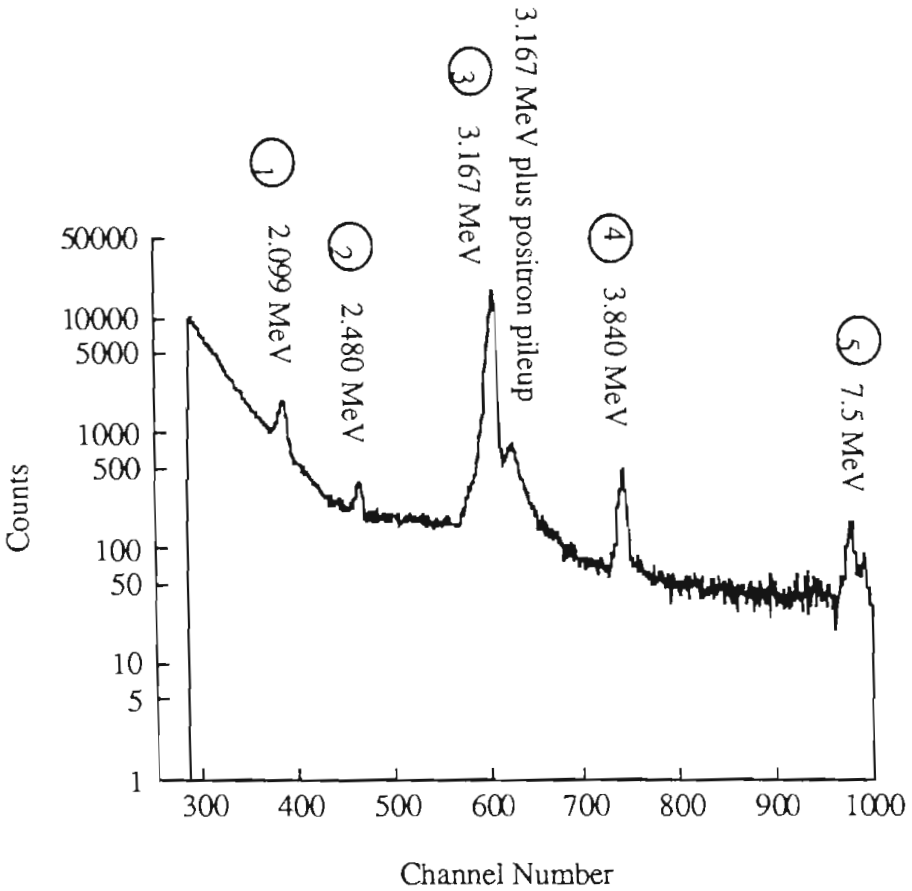

Figure 3.4. Proton singles spectrum. The energies of the numbered peaks are taken from (Bor87). Peak [3] corresponds to protons from the decay of the T=3/2 state at 5.55 MeV excitation in ^{33}Cl. Note the positron pileup peak.

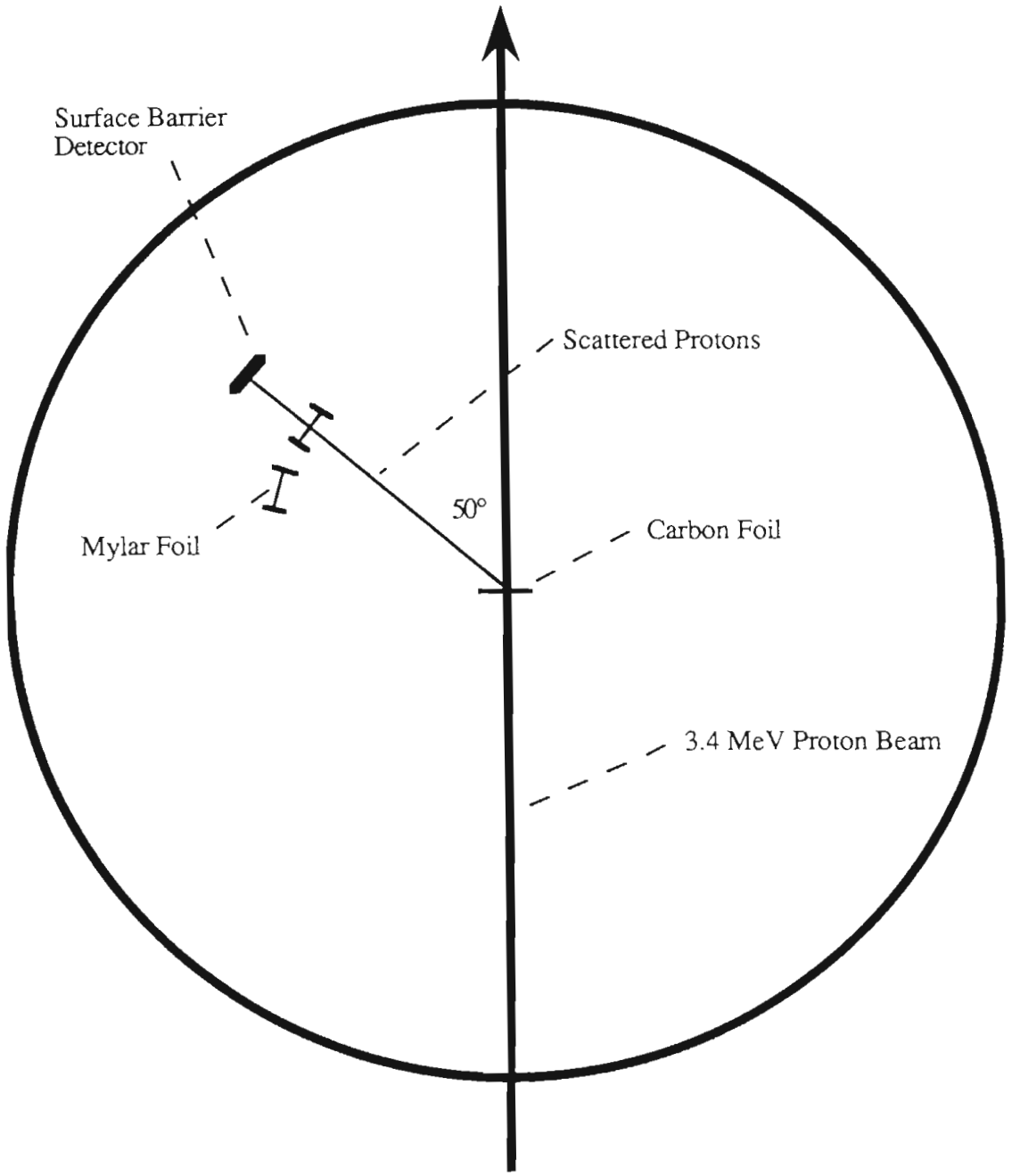

Figure 3.5. Scattering chamber setup for the mylar foil thickness measurements. Each foil was rotated in turn to intercept protons scattered into the detector. The detector collimation is not shown.

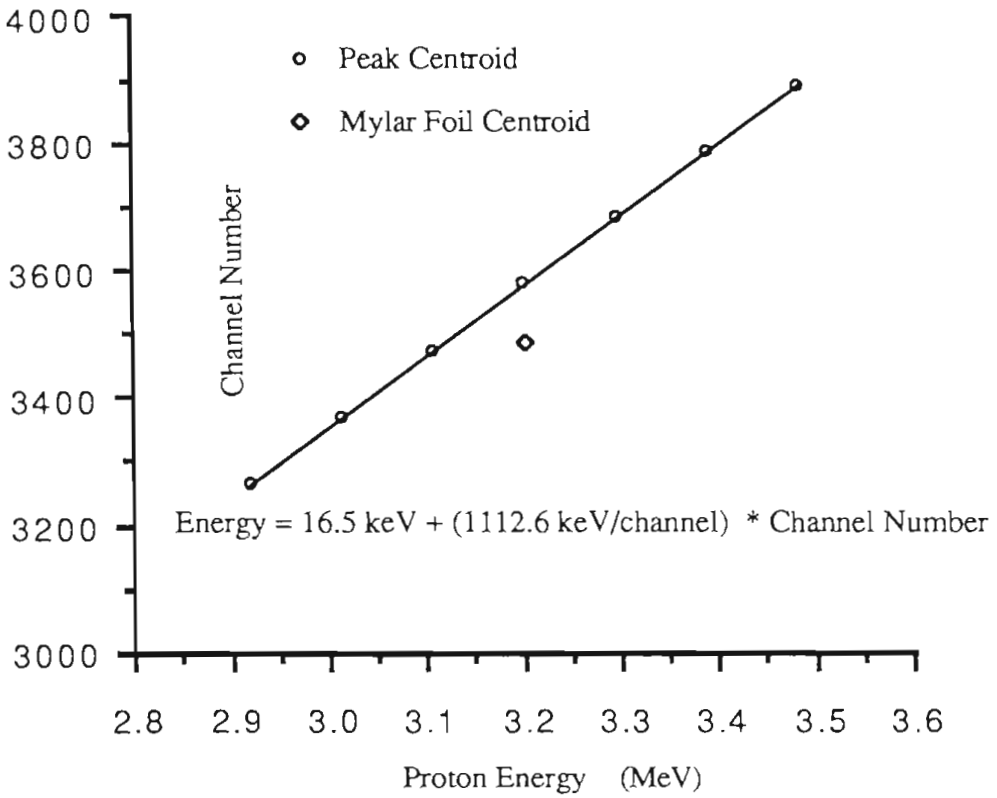

Figure 3.6. Determination the energy lost by 3.2 MeV protons in the mylar foil. The energy loss is the vertical distance between the point labeled "Mylar Foil Centroid" and the fit to the "Peak Centroid" points, 82.6 $\pm$ 1.0 keV.

each region using the relativistic Bethe equation, which is based on the Born approximation of a heavy particle interacting with atomic electrons (Bet53). The energy losses suffered by the other proton groups were then calculated from the thickness of the foil.

The gains of the surface barrier detectors and electronics during the production run were monitored by taking the centroid of each 3.2 MeV singles proton peak for each run. Gain shifts of a few keV over several days were observed (see Figure 3.7). There were, in addition, four gain changes caused by replacement of detectors or malfunctioning electronics. The small shifts were accounted for off-line by subtracting a constant from the data for each detector for each run, so that the centroids of each 3.2 MeV peak lay in the same channel. The detector gains for each series of runs were then determined from the energies and positions of the proton peaks labeled 2, 3, and 4 in Figure 3.4.

The scintillator gain shifts were monitored during data taking by collecting daily spectra from ^{22}Na, ^{60}Co, ^{207}Bi, and ^{137}Cs gamma-ray sources and determining the position of the Compton edges for each γ-ray energy present (Table 3.1). Background spectra, presumably stable in character and dominated by 511 keV positron annihilation photons, were also collected. At the end of the data taking the ^{33}Ar gas cell was replaced by the ^{207}Bi source and the electron conversion line spectrum was recorded under the same conditions as the ^{33}Ar data, with the exception that the interface was activated by telescope coincidences rather than silicon detector signals. The centroid of the most prominent (K- and L-shell) conversion lines is 990 keV (Led78).

During off-line data analysis the endpoint of the ^{33}Ar positron spectrum was determined through use of a Kurie plot (Figure 3.8). For an allowed transition the energy spectrum of the emitted beta particles is

$$N(E_e) = F(E_e)\, E_e \sqrt{\left(E_e^2 - m_e^2\right)}\, (E_0 - E_e)^2, \qquad (3.1)$$

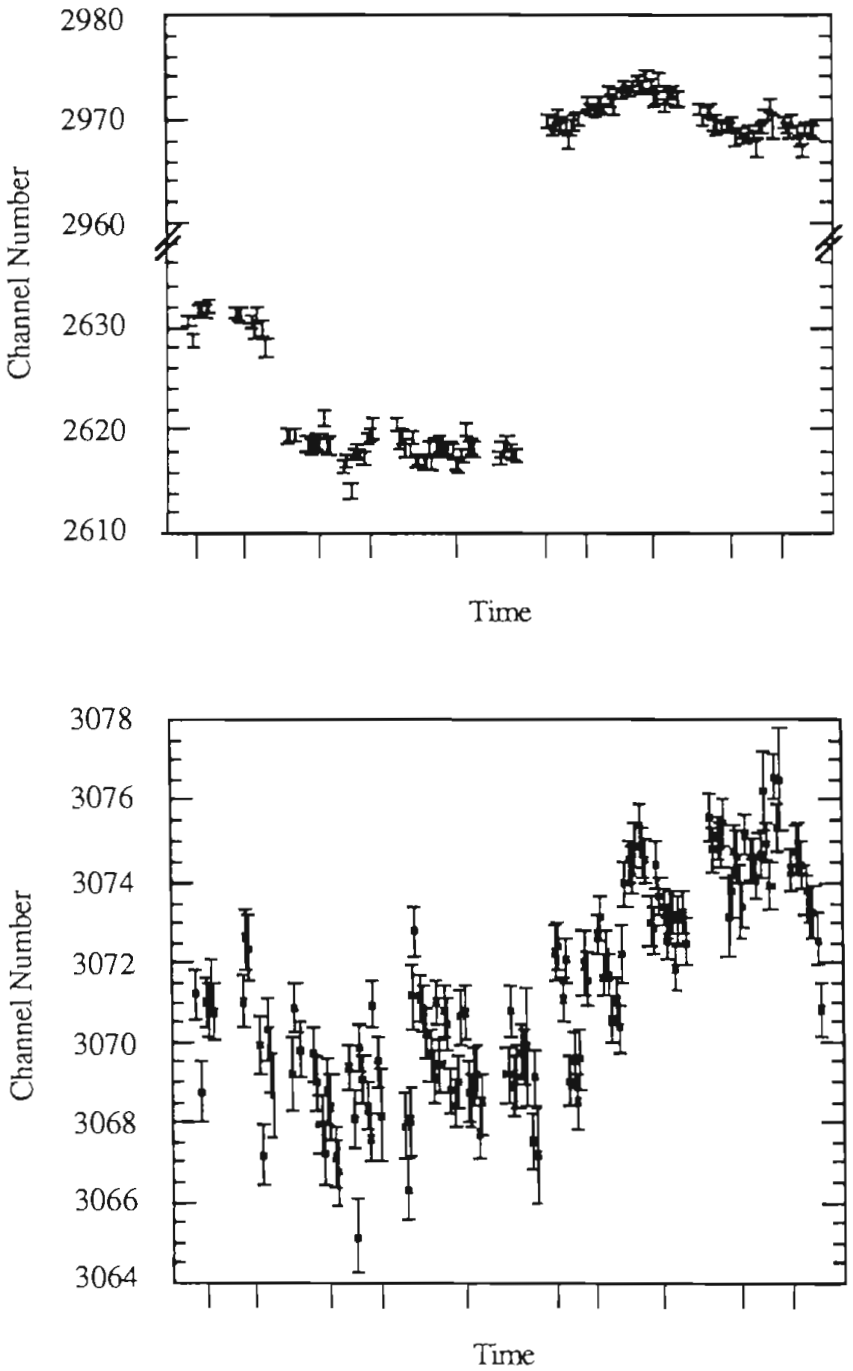

Figure 3.7. Gain shifts for surface barrier detectors one (top graph) and four (bottom). The large gain changes in detector one correspond to replacement of electronics or the detector. Gains are typically 1 keV/channel. The hashmarks on the horizontal scale correspond to midnight of each day.

Table 3.1. Parent nuclei, transition energy, and Compton edge energy of the transitions used to monitor the scintillation detector gains.

Parent Nucleus	Transition Energy (keV)	Compton Edge Energy (keV)	Relative Intensity
^{22}Na	1274.5	1061.7	
^{60}Co	1332.5	1118.1	100
	1173.2	963.4	99.9
^{137}Cs	661.7	477.4	
^{207}Bi	569.7	393.3	97.9
	1063.6	857.6	75.5

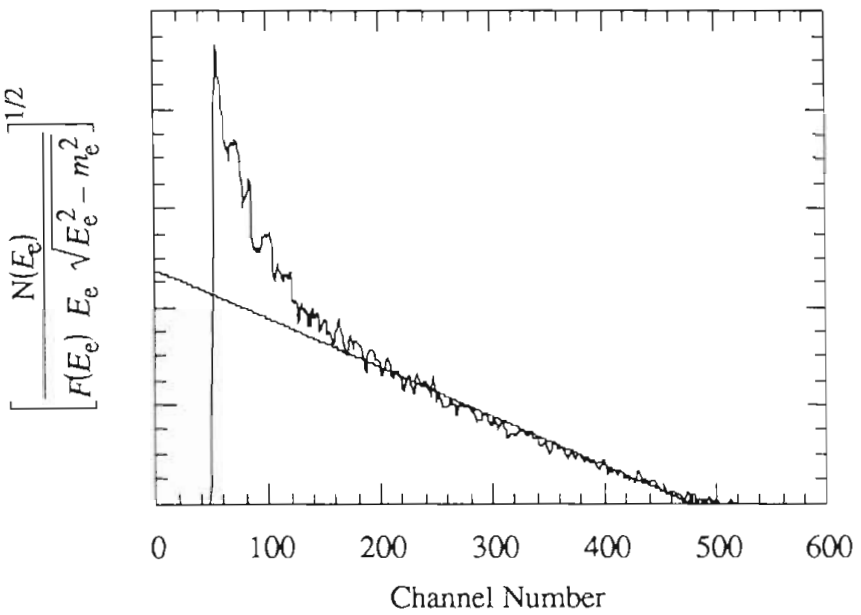

Figure 3.8. Kurie plot of the positron spectrum of ^{33}Ar in counter number 4.

where E_e is the total electron (or positron) energy, p is the electron momentum, E_0 is the energy endpoint, and $F(E_e)$ is the Fermi function. The Fermi function is the number of states available to the leptons. A Kurie plot is a graph of

$$E_e \text{ vs. } \left[\frac{N(E_e)}{F(E_e)\ E_e\ \sqrt{E_e^2 - m_e^2}}\right]^{1/2} \tag{3.2}$$

which yields a straight line that intercepts the energy axis at E_0. A Kurie plot can be used either to determine the endpoint of a beta-decay transition when the detector calibration is known or, as in our case, can be used to calibrate a detector when the endpoint energy of the transition is known.

Our use of the Kurie plot is complicated by the gamma rays resulting from positron annihilation. Some of these photons undergo Compton scattering inside the scintillator, thus depositing energy in the detector. To estimate the magnitude of this effect a Monte Carlo simulation of the interaction of the photons with the scintillator was performed (Figure 3.9). It was found that for roughly 1/3 of all events one or both of the annihilation photons interacted with the scintillator, depositing an average energy of 200 keV. This produced the distortion of the Kurie plot evident in figure 3.8.

To correct this distortion a modified version of the Kurie plot was developed. The measured positron energy spectrum was assumed to be

$$\begin{aligned} N(E_e) &= \left\{\alpha\, F(E_e)\, E_e \sqrt{\left(E_e^2 - m_e^2\right)}\right\}(E_0 - E_e)^2 + \\ &\left\{(1-\alpha)\, F\left(E_e - E'\right)\left(E_e - E'\right)\sqrt{\left[\left(E_e - E'\right)^2 - m_e^2\right]}\right\}\left(E_0 - E_e + E'\right)^2 \\ &\equiv \{A\}(E_0 - E_e)^2 + \{B\}\left(E_0 - E_e + E'\right)^2 \end{aligned} \tag{3.3}$$

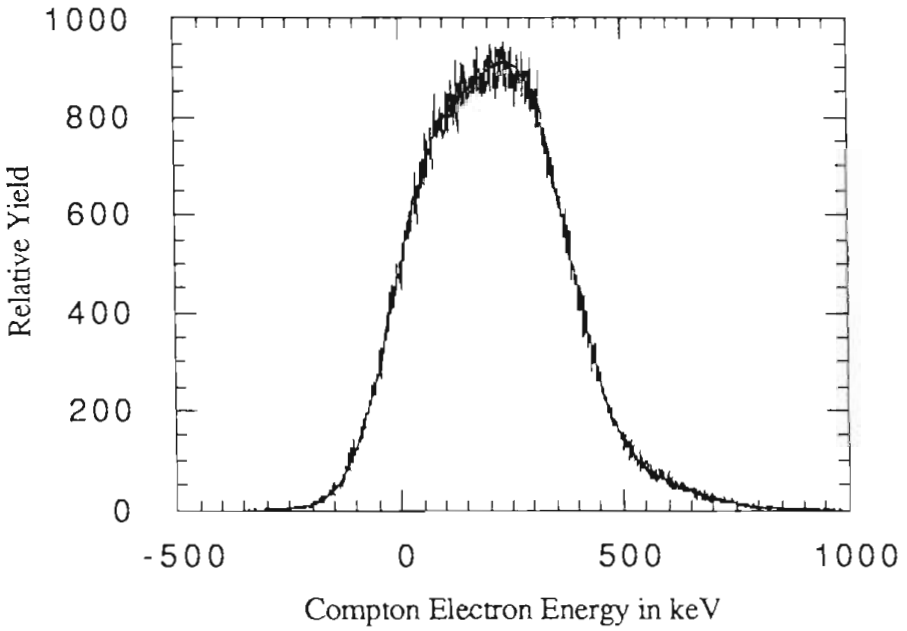

Figure 3.9. The Compton electron energy spectrum as determined by Monte Carlo modeling. The detector resolution was assumed to be 200 keV. A fit of the spectrum consisting of three Gaussians is also graphed.

where $E' = 200$ keV and $1 - \alpha \approx 0.3$ is the fraction of events which are accompanied by Compton scatterring. This equation can be rearranged to produce $E_0 - E'$ as a funtion of $N(E_e)$, a, and E':

$$E_0 - E_e = \frac{-B\,E' + \sqrt{(A+B)\,N(E_e) - A\,B\,E'}}{(A+B)} \qquad (3.4)$$

A plot of the right hand side of Equation 3.3 vs. E_e again yields a straight line which intercepts the horizontal axis near E_0 (Figure 3.10). The gains of the detectors during the run were then derived from a linear fit to the ^{33}Ar endpoints determined from the modified Kurie plots, the Compton edge spectra, and the ^{207}Bi conversion line spectra. This fit is graphed in Figure 3.11.

Section 3.5. Response of Telescopes to Positrons.

To determine the response of the telescopes the spectra of several positron emitters were taken with the detector geometry which was similar to that which was employed during the production run. The principal differences were that during the calibration run the counting chamber was placed on the beam line, the counting cell was replaced by a solid target, and only one telescope was used The positron emitters, listed in Table 3.2, were produced by (p,n) reactions on the daughter nuclei. This set of transitions was selected because their beta-particle energy endpoints vary over a useful range (1 to 5 MeV), they have half-lives of several seconds, there is only one strong decay branch for each parent, and the sources can be produced from compounds from which no other positron emitters with half-lives comparable to the transition of interest are made.

The conversion gain of the detection system was calculated from the endpoints of each spectrum as determined from modified Kurie plots (figure 3.12) and the Compton edges of gamma rays emitted from ^{137}Cs, ^{207}Bi, and ^{22}Na sources. The calibration is

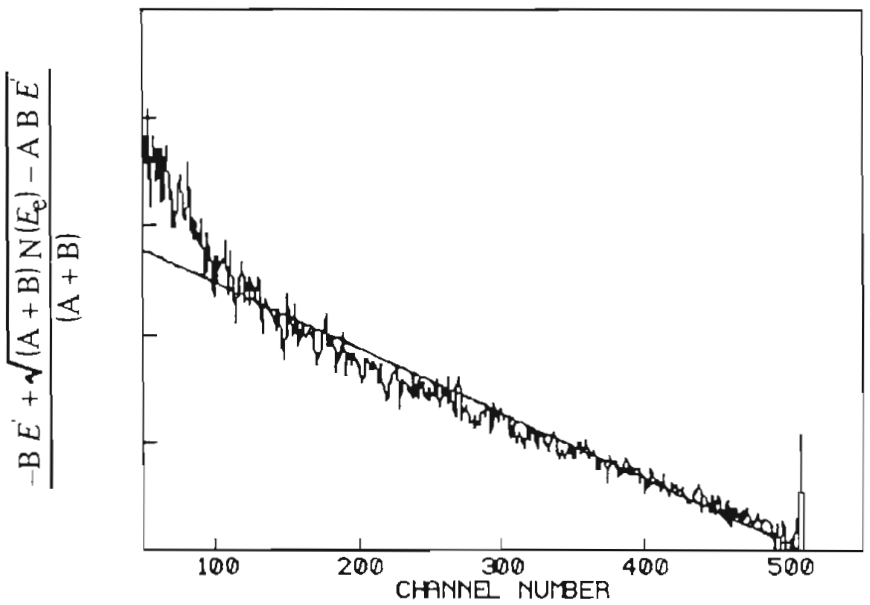

Figure 3.10. Modified Kurie plot of ^{33}Ar for detector 4.

Table 3.2. Daughter nuclei, positron endpoint energies, and branching ratios of the transitions used to determine the response function of the scintillation detectors.

Parent Nuclei	Daughter Nuclei	Positron Energy Endpoint (MeV)	Branching Ratio (%)
^{19}Ne	^{19}F	2.216	99.10
^{23}Mg	^{23}Na	3.037	91.4
^{27}Si	^{27}Al	3.787	99.77
^{35}Ar	^{35}Cl	4.943	98.3

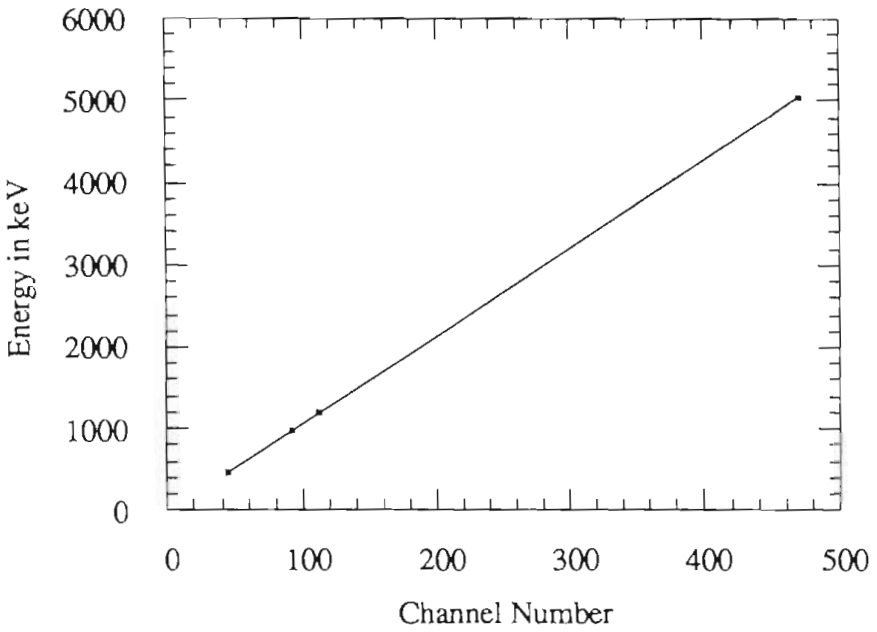

Figure 3.11. The calibration of beta counter 4. The points are derived from the Compton edges of annihilation photons and gamma rays emitted from ^{22}Na and ^{207}Bi sources, and the endpoint of the ^{33}Ar spectrum as determined from a modified Kurie plot.

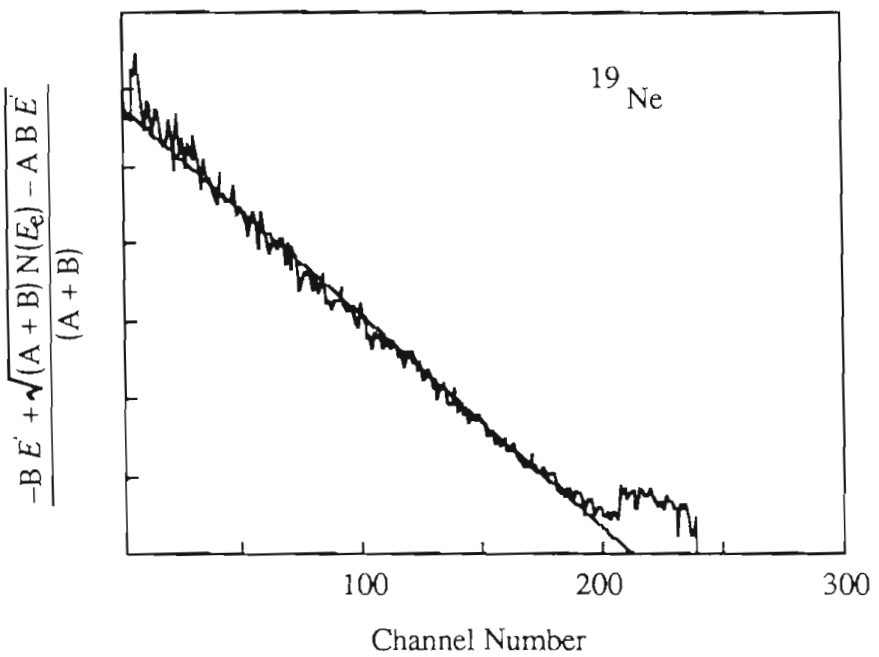

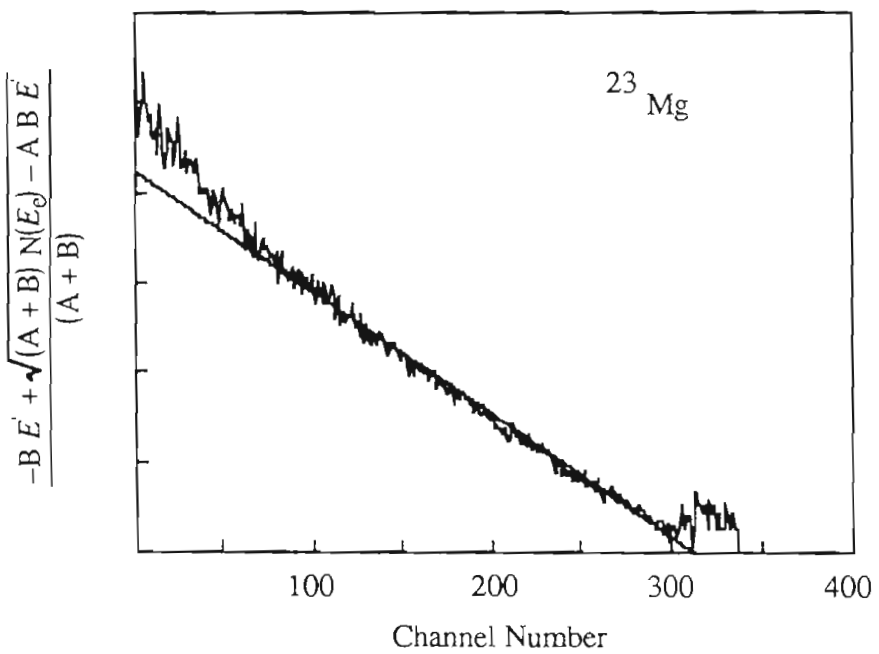

Figure 3.12a). Modified Kurie plots of spectra acquired to determine the scintillator response function.

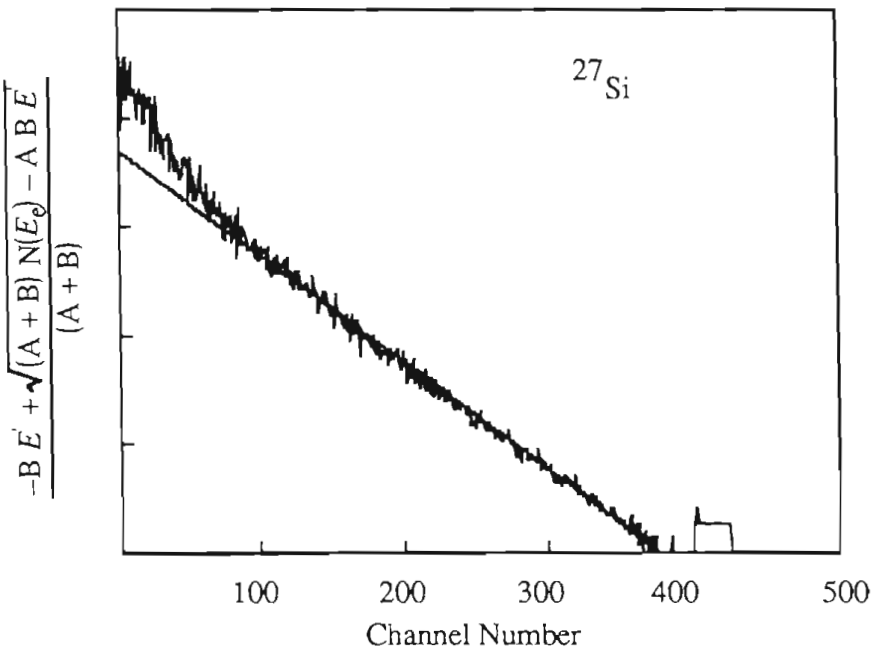

Figure 3.12 b). Modified Kurie plot of ^{27}Si.

graphed in Figure 3.13. The collected spectra were then fit with a sum of four Gaussians and a flat low energy tail using the minimization program MINUIT (Jam75). The form of the fitting function was suggested by the Monte Carlo simulation of the Compton scattering of the annihilation photons (Figure 3.9) and the work of Clifford (Cli89), who determined the response to positrons of telescopes similar to ours. The first of the four Gaussians corresponds to positrons which deposit their full energy in the scintillator. The other three correspond to events in which one (or both) of the annihilation photons Compton scatters in the detector. The low energy tail is the result of events in which the positrons deposit only part of their energy in the scintillator, either because they scatter out of the detector or annihilate in flight. The free parameters of the fit are the width and fractional yield of the first Gaussian. The widths, fractional yields, and postions of the other three Gaussians were determined (relative to the width, yield, and position of the first Gaussian) from the Monte Carlo simulation but were allowed to vary around their initial values. The fitted values of the fourteen parameters and the shape of the resulting distribution function are presented in Figure 3.14. In Figure 3.15 the data and fit are graphed for each transition.

Section 3.6. Conclusion.

The equipment and procedures outlined in Sections 3.2 and 3.3 were designed to collect events which would allow the angular correlation coefficient for the decay of ^{33}Ar to be extracted using the method of Section 2.3. The ^{33}Ar was produced via ^{32}S(^{3}He,2n) and transported from the beam line to a low-background counting chamber by a helium carrier gas system. Four detector telescopes consisting of a thin suface barrier detector backed by a scintillation detector were used to collect and record th energies of coincident protons and positrons emitted at relative angles of 90° and 180°. The analysis of these data, which consisted of extracting a set of proton energy shifts as a function of positron energy from

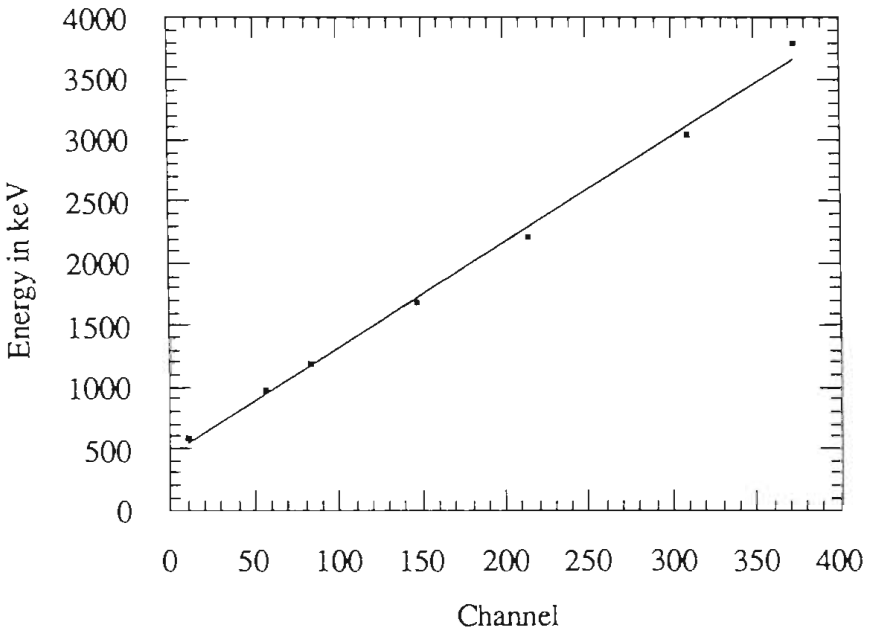

Figure 3.13. Energy calibration of the scintillation detector used to determine the response of the telescopes to positrons. The three points with energies greater than 2000 keV were derived from the endpoints of the positron spectra of ^{19}Ne, ^{23}Mg, and ^{35}Ar. The other four points were determined from the Compton edges of photons emitted following the decay of ^{207}Bi, ^{137}Cs, and ^{22}Na.

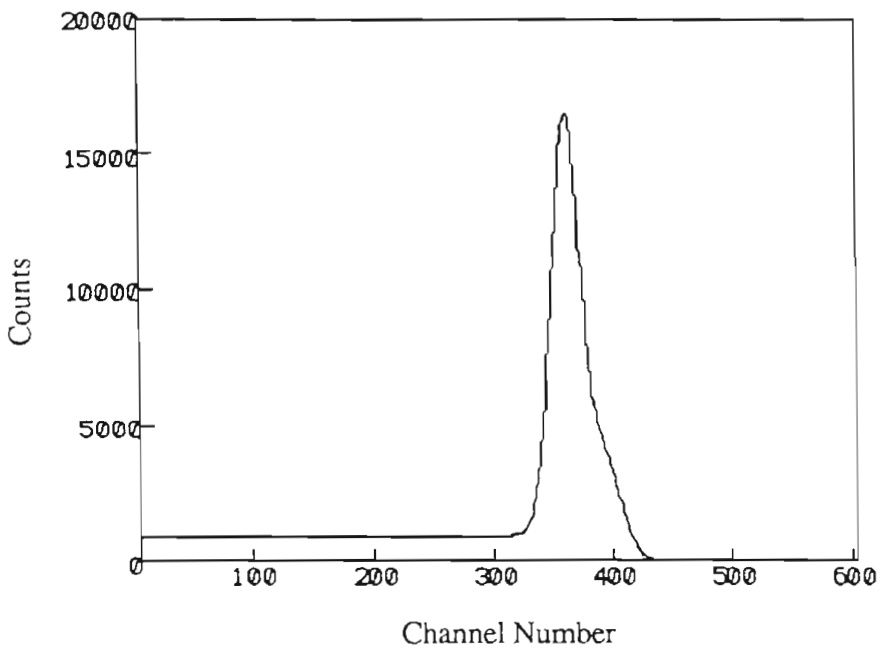

Figure 3.14. The scintillation detector response to positrons. The graph is for a monoenergetic beam of positrons with a total energy of 4.1 MeV.

The parameters of the response function are:

Fraction of counts in the full energy peak

$F_0 = 0.51 - 4.5 \times 10^{-3} E + 1.5 \times 10^{-2} E^2$ with E given in MeV.

Fraction of counts in the the three annihilation peaks:

$F_1 = 0.37\ F_0$, $F_1 = 0.61\ F_0$, $F_1 = 0.02\ F_0$.

Width of full energy peak:

$W_0 = 76 + 6.7 \times 10^{-2} E$ (W_0 in keV, E in MeV).

Partial width of the annihilation peaks:

$W_1 = 39$ keV, $W_2 = 74$ keV, $W_3 = 68$ keV.

Position of annihilation peaks relative to full energy peak:

$P_1 = 71$ keV, $P_2 = 270$ keV, $P_3 = 570$ keV.

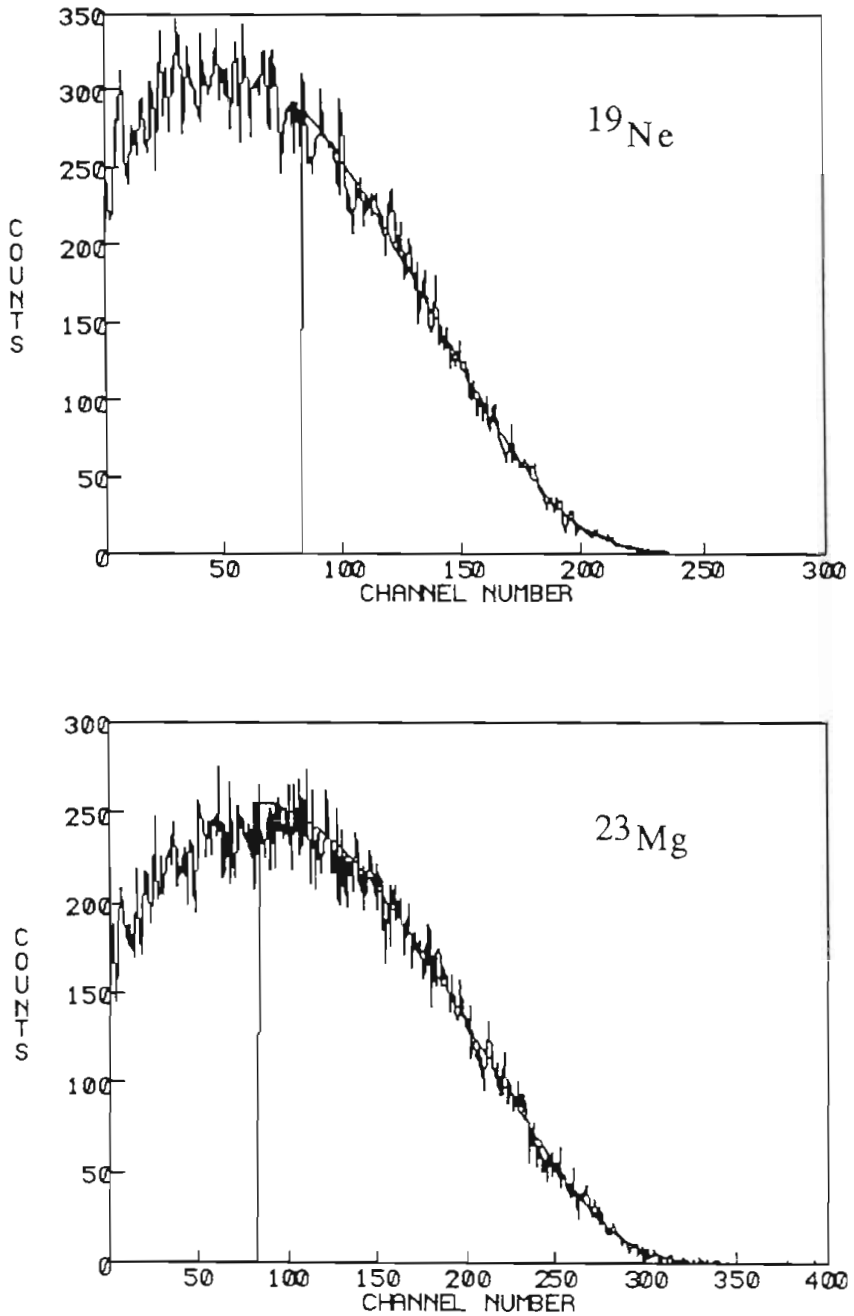

Figure 3.15 a). Fits to the positron spectra of ^{19}Ne and ^{23}Mg.

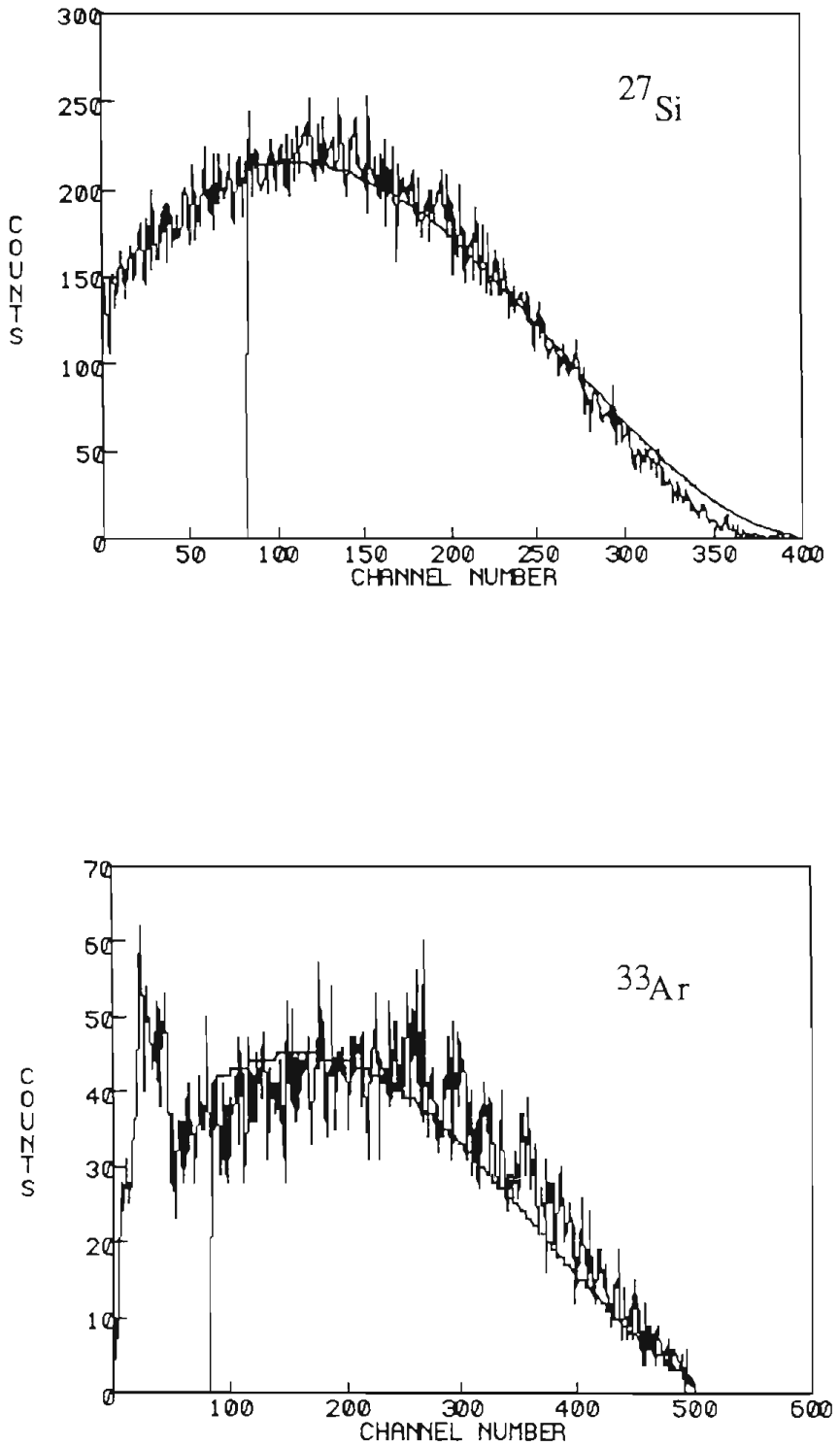

Figure 3.15 a). Fits to the positron spectra of ^{27}Si and ^{33}Ar.

the data and performing a Monte Carlo simulation of the experiment, is explained in Chapter 4.

Chapter 4. Data Analysis and Discussion.

Section 4.1. Introduction.

This chapter presents the methods used to reduce the data collected according to the procedures of Chapter 3 to a set of proton energy shifts as a function of beta-particle energy (Section 2), the extraction of the correlation coefficient by comparing the data to a Monte Carlo simulation of the experiment (Sections 3 and 4), and the calculation of limits on the scalar coupling strength and the Gamow-Teller transition strength (Section 5). Conclusions from the experiment are recorded in Section 6.

Section 4.2. Data Reduction.

As explained in Section 3.3, the collected data were stored event by event on magnetic tape for later analysis. The data for each event consisted of 13 two-byte words, which contained the digitized signals for the four surface barrier detectors, four scintillation detectors, four TACs, and the detector routers.

The analysis required several data sorts. The first sorts were made to check detector gain and electronic timing stability and to determine the regions of interest in each spectrum for later sorts. A sort was also performed to test for event mixing of the type described in Section 3.3.

The logic of the final sort is reproduced in Figure 4.1. The surface barrier detector energy signal for each event is sorted into one of 40 spectra, provided a valid positron energy signal is received with the proper timing (as determined from the appropriate

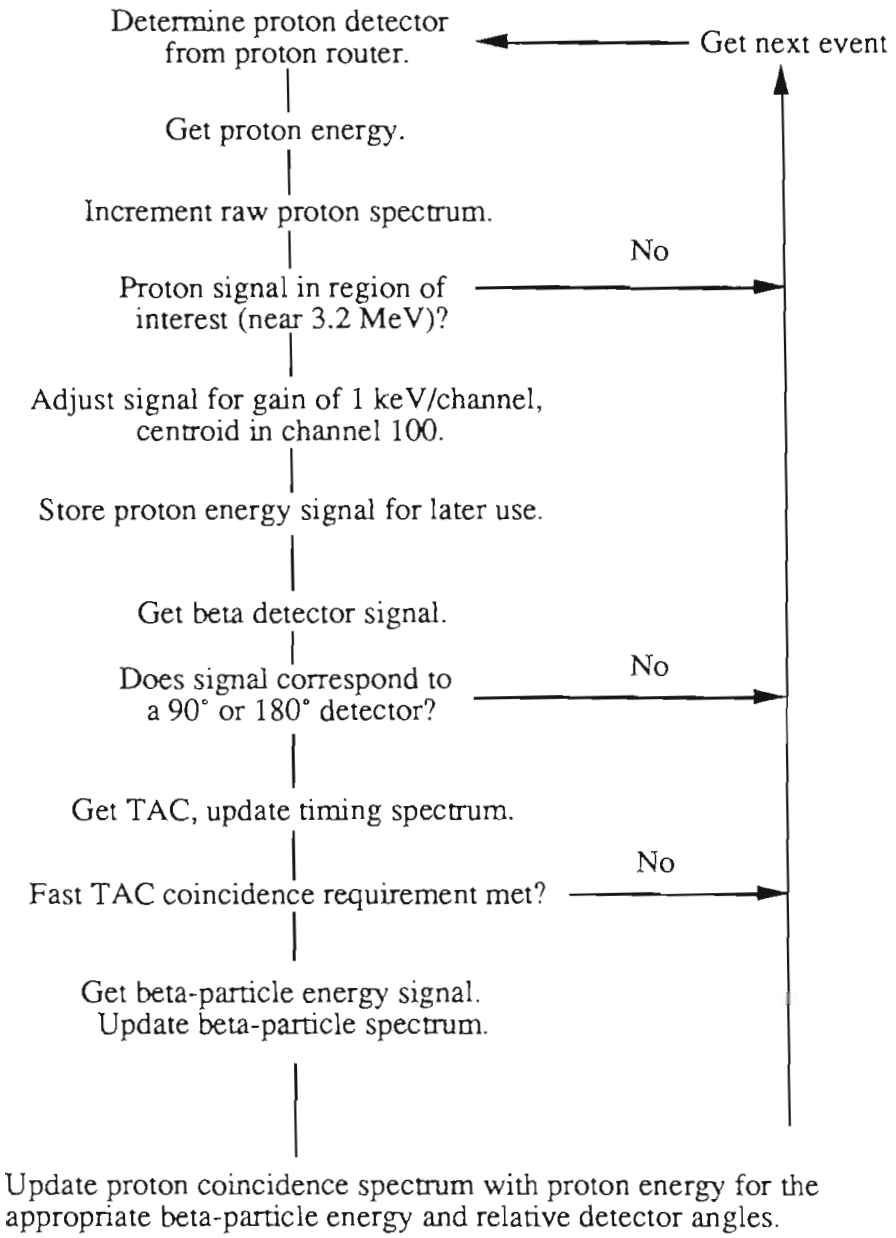

Figure 4.1. Logic flowchart of the data sorting program.

TAC). The spectra were selected according to the energy of the positron (each spectrum corresponded to a 250 keV bin in the beta-particle energy) and the detection geometry (perpendicular or antiparallel). The channel numbers of the proton energy signals in events which passed these criteria were "normalized" by subtracting the channel number of the centroid of the proton singles peak from the digitized signal, dividing by the detector gain in keV/channel, and adding 100. The end result was therefore 40 spectra each with a gain of 1 keV. An "unshifted" proton peak would be centered on channel 100.

Since events detected in the perpendicular geometry have only a very small shift the perpendicular spectra were added together and the centroid of the resulting peak was determined. The centroids of the antiparallel proton peaks were also calculated. The differences of the centroids of each of the antiparallel peaks with the (total) perpendicular peak are the proton energy shifts.

Section 4.3. Monte Carlo Simulation.

The equation relating the shifts to a, Equation 2.9,

$$\overline{\Delta E}_{\hat{p}} = \frac{1}{2}\frac{m_p}{m_{Cl}{}^2}\left(p_\beta{}^2 + p_\nu{}^2 + a\,\frac{v}{c}\,\frac{2}{3}\,p_\beta p_\nu\right) - \frac{p'\cos\alpha}{m_{Cl}}\left(p_\beta + \frac{a}{3}\,\frac{v}{c}\,p_\nu\right), \qquad (2.9)$$

is not complicated, however the extraction of the correlation coefficient from the shifts is not a trivial matter because of experimental complications.

The first of these complications is the finite detector and cell geometry. While the shifts of Figure 2.2 were calculated for protons and positrons emitted in exactly opposite directions, a large range of relative emission angles contributed to the collected data. This reduces the average shifts relative to the curves of Figure 2.2.

A second complication results from the mylar foil of the gas cell, which absorbs energy from the protons as they pass through. While it would appear that since both perpendicular and antiparallel protons pass through the foil, the energy shift (the difference of the energies of the two sets of protons) is not affected by the foil, this is not exactly correct because of the coincidence requirement. A pair of perpendicular telescopes will be more likely to see a decay in the near corner of the cell than in the center or far corner. The probability of detection in a pair of antiparallel detectors is more even throughout the cell. Therefore the two geometries see slightly different populations of decay positions within the cell and the average angle at which the protons traverse the foil is also different. The energy loss for 3-MeV protons passing through a 6 μ mylar foil is proportional to the thickness of foil traversed, hence the average energy lost by protons detected in the two geometries is not equal. This introduces an additional energy difference between perpendicular and antiparallel protons which is constant for all beta-particle energy bins.

Finally, the scintillator response function affects the shape of the proton energy shift vs. beta-particle energy curve. Because events with a large range of actual positron energies contribute to the data of each bin, convolution of the beta spectrum with the response function tends to flatten the curve.

To account for these experimental complications a Monte Carlo simulation of the experiment was performed. The logic of the simulation is presented in the flow chart of Figure 4.2. The inputs to the simulation consisted of the cell and detector geometry, scintillator response function, cell wall thickness, correlation coefficient, and silicon detector resolution. The direction of proton, positron, and neutrino emission, the positron energy, and the scintillator and surface barrier detector responses were drawn

randomly from the appropriate probability distributions. The simulation then calculated the spectra

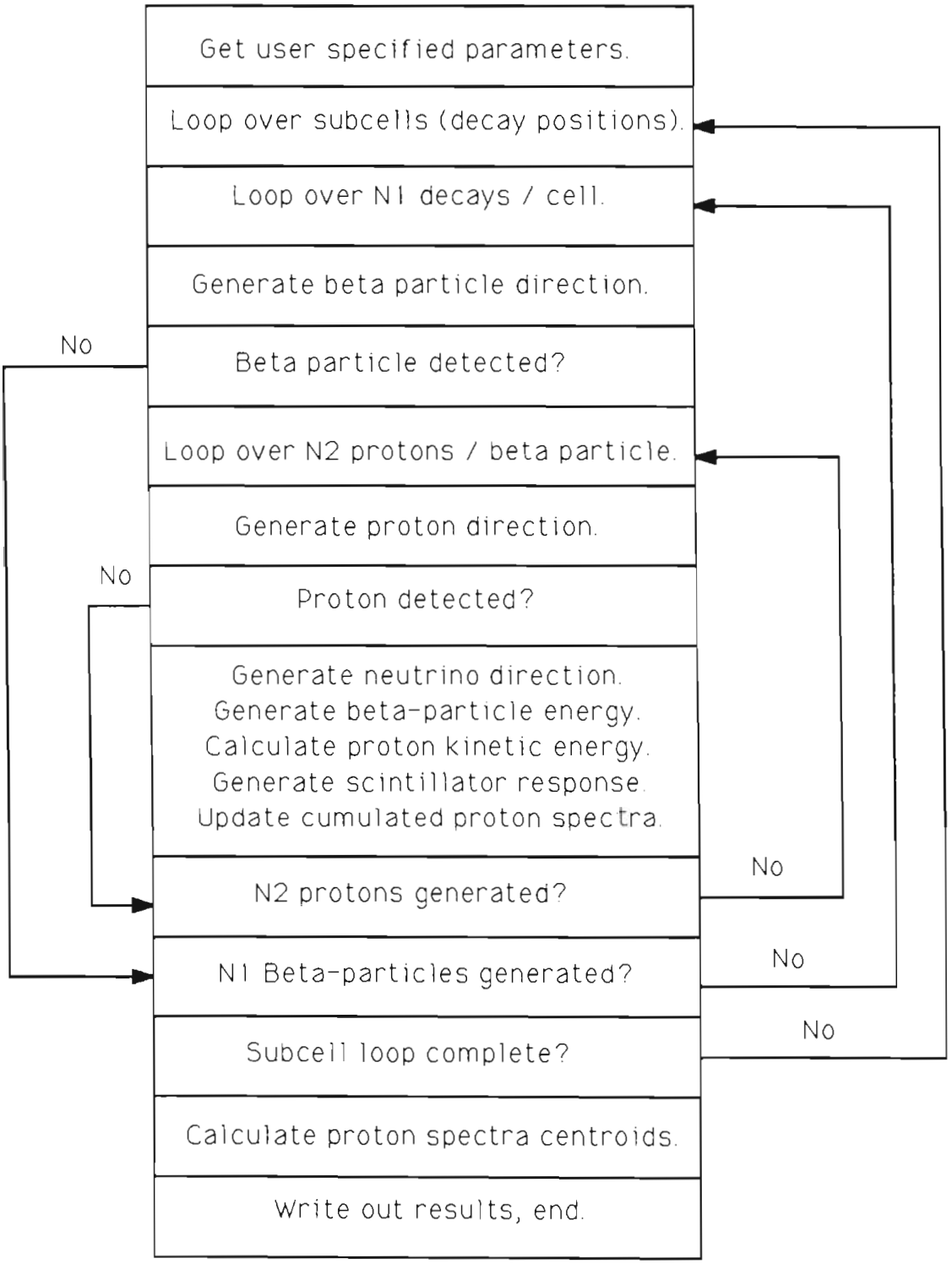

Figure 4.2. The logic of the Monte Carlo simulation. The number of source subcells and 33Ar decays per cell are supplied by the user. The number of protons generated per detected positron is a function of the geometry.

of protons for the (detected) positron energy bins specified by the user. The calculated energy shifts for varying values of the correlation coefficient were then compared to the data to determine the beta-neutrino angular correlation. An example of the dependence of the calculated energy shifts vs. positron energy on the angular correlation coefficient is shown in Figure 4.3.

Proper implementation of the Monte Carlo method requires both careful testing of the program and accurate determination of the input parameters. Programming errors, selection of random numbers from improper probability distributions, or inaccurate assumptions regarding the physical parameters introduce errors which may be quite subtle. Our testing consisted of running the Monte Carlo program with a set of simplifying physical assumptions so that the results could be compared with energy shifts calculated analytically. Realistic physical parameters were then gradually introduced to the program to insure that the effect of each input on the results was appropriate.

The initial simplifying program assumptions were:

- ideal (delta function) scintillator response;

-point ^{33}Ar source;

-zero mylar foil thickness;

-delta function positron energy distributions.

Ten simulations were performed in which the positron energy was varied from 0.0 MeV to 5.0 MeV in 0.5 MeV steps. The results of these calculations could be compared directly with an analytic calculation of the shift for the case in which the positron and proton are emitted exactly antiparallel, with an allowance made for the finite detector geometry assumed in the program. Note the dependence of the proton energy shift on α, the relative proton-positron emission angle, in Equation 2.9. Protons emitted exactly

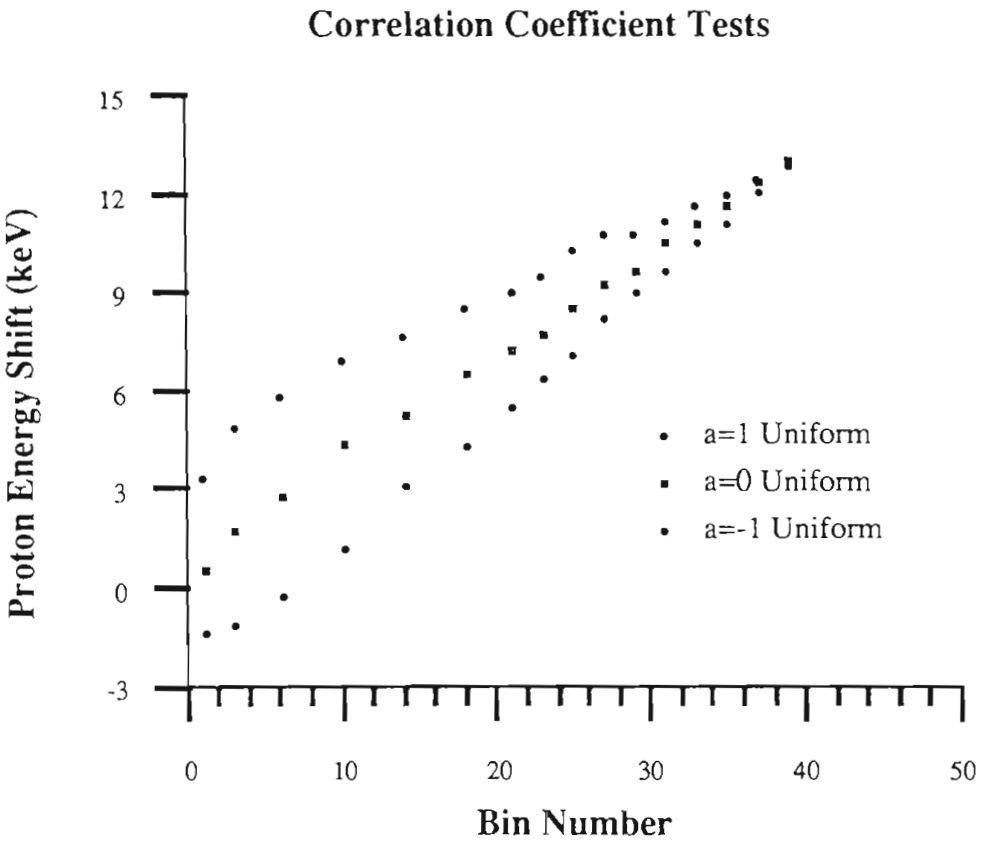

Figure 4.3. Example of the dependence of the calculated proton energy shifts on beta-particle energy and correlation coefficient. Each bin on the horizontal axis contains results for events with positron energy in a 250 keV range (so that bin number 1 contains events with 0 keV < positron energy < 250 keV). Positron energies were drawn from an (unphysical) uniform distribution rather than the proper Fermi distribution in order to acquire adequate statistics for the lowest and highest bins as well as those around bin 10.

antiparallel to the positrons have the maximum average energy shift, therefore use of finite sized detectors must produce smaller energy shifts than the analytic calculation. The dependence of the energy shift on the solid angle subtended by the detectors was observed by changing the distance between the detectors and source or, equivalently, the detector size. The results of these tests, presented in Table 4.1, indicate that the kinematic calculations are being performed properly.

The next step was to introduce more realistic parameters to the program one at a time. Introducing a foil with a thickness of 6.35 microns degraded the energy of both perpendicular and antiparallel protons equally, with no change in the energy shifts. This was to be expected for a point source, since protons from both perpendicular and antiparallel coincidences pass through the foil almost normally. As noted above, this is not necessarily true for emission from an extended source from which the protons could traverse the cell walls at a range of angles.

Two continuous positron energy distributions were then introduced. These were the uniform distribution and the allowed Fermi distribution. The proton energy shifts for each positron energy bin are graphed in Figure 4.4 along with the delta function results. The differences between the results obtained with these three distributions are small, implying the results for the continuous distributions are consistent with the delta function results.

The next test was to distribute the ^{33}Ar decay position evenly throughout the cell. Since this further relaxes the geometric constraints required for coincidence, the magnitudes of the shifts for each beta-energy window were reduced by a roughly constant factor. The results, calculated for a Fermi energy distribution, are graphed in Figure 4.5.

The next test consisted of introducing the actual scintillator response function This produces a flattened energy shift curve (Figure 4.6). This was expected, since each (detected) energy bin now contains a mixture of all (actual) positron energies.

The final test consisted of varying the thickness of the mylar foil for the extended cell geometry. It was found that a foil with a thickness of roughly 6 microns produced an energy shift of the order of one keV (Figure 4.7) and therefore the foil thickness was determined to within a few percent (see Section 3.4).

Table 4.1. The results of the simplified Monte Carlo simulation of the experiment compared with the analytic calculation of the shift. The simplifying assumptions made were: delta function beta detector response, point ^{33}Ar source, zero energy loss in the mylar wall of the gas cell, and delta function beta-particle energy spectra. The difference between the simulation and analytic energy shifts is a result of the finite detector size assumed in the simulation.

Positron Energy	Simulation Shift (keV)	Analytic Shift (keV)	Simulation / Analytic (%)
0.5	4.90	5.33	92.9
1.0	6.37	6.68	95.4
1.5	7.28	7.70	94.5
2.0	8.12	8.63	94.1
2.5	8.94	9.52	93.9
3.0	9.77	10.40	93.9
3.5	10.60	11.27	94.1
4.0	11.47	12.13	94.6
4.5	12.17	12.99	93.7
5.0	13.04	13.85	94.1

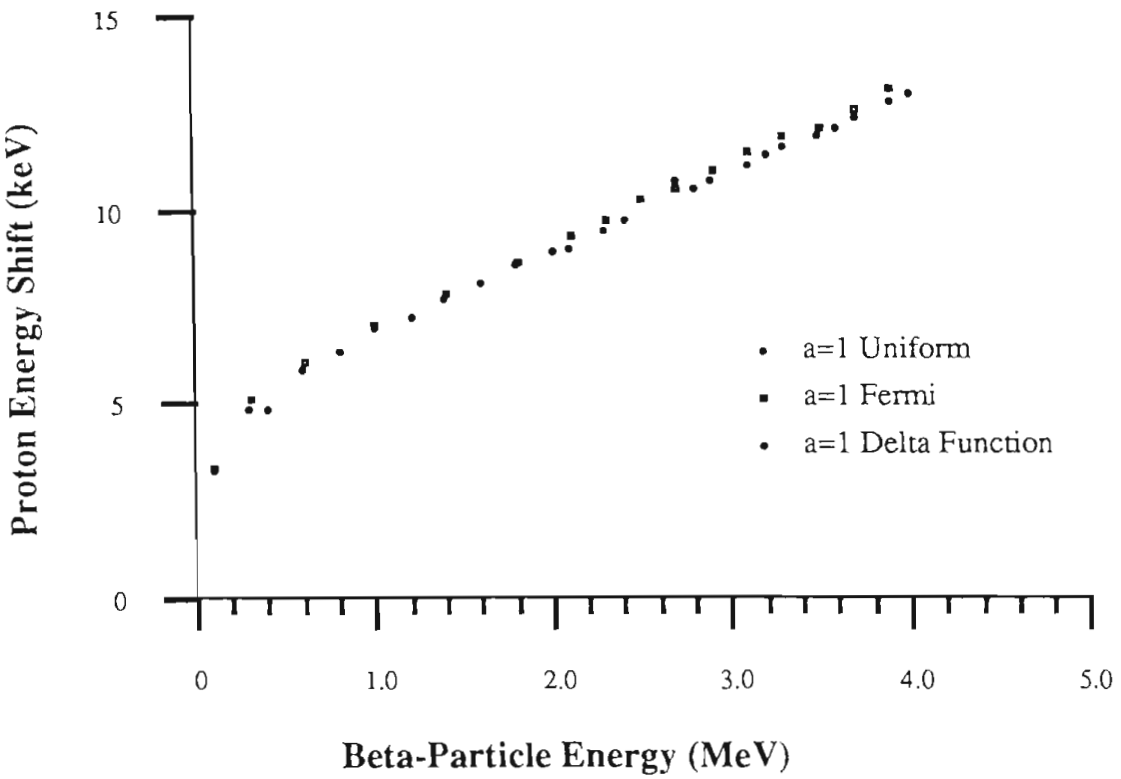

Figure 4.4. A comparison of the proton energy shifts produced by the Monte Carlo simulation for three different beta energy spectra.

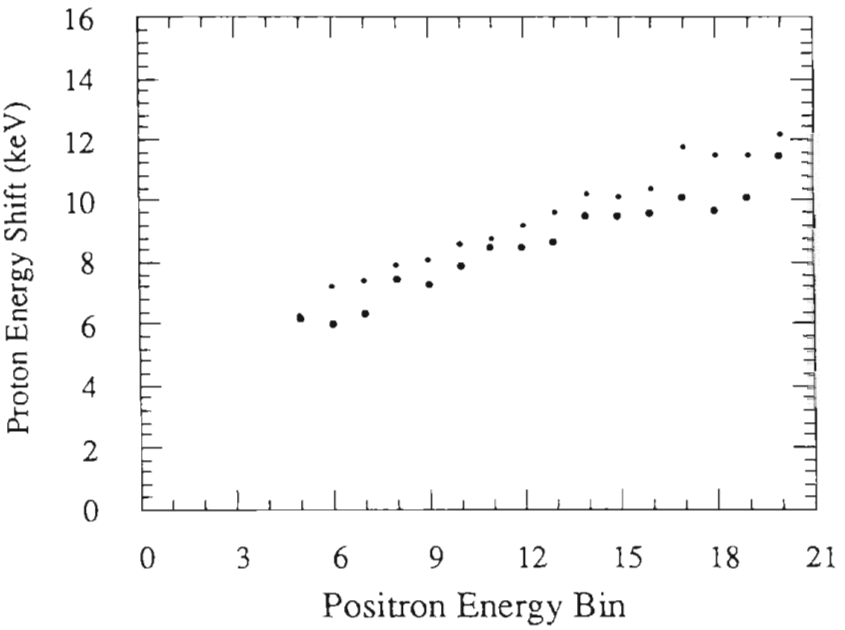

Figure 4.5. Comparison of proton energy shifts calculated for point and extended source geometry. The extended geometry (closed squares) produces consistently smaller shifts than the point source geometry (crosses).

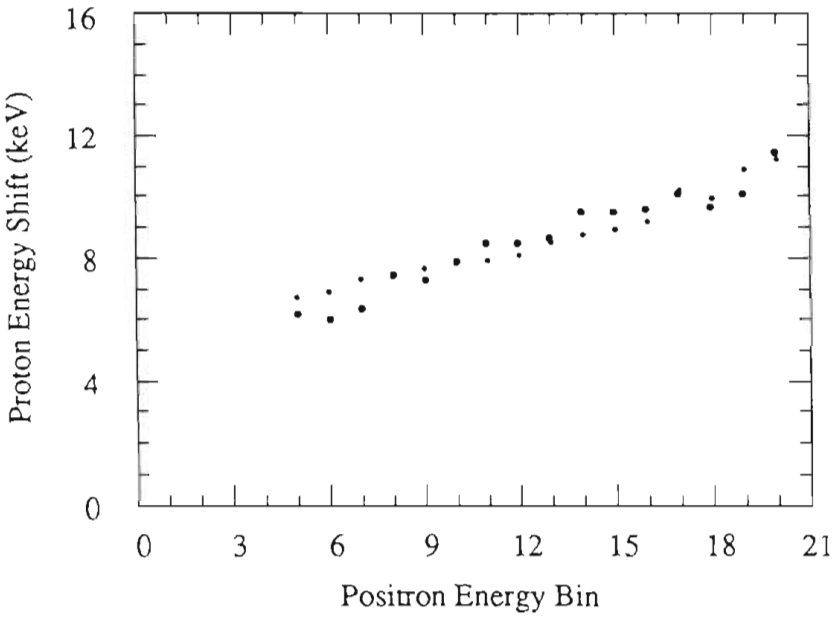

Figure 4.6. The effect of a realistic detector response function on the proton energy shifts. The realistic response (crosses) causes the events with a given positron energy to be spread among many bins, thus 'flattening' the proton energy shift vs. positron energy curve relative to the results for a delta function response (closed squares).

Section 4.4. Extraction of Centroids from the Spectra.

With the Monte Carlo simulation tested and the physical parameters of the apparatus determined the extraction of the angular correlation coefficient should be straightforward. The simulation was run for various values of a, and the experimental and calculated proton energy shifts are compared. Unfortunately it was found that the beta-particle energy spectrum produced by the calculation disagreed with the measured spectrum. Agreement was obtained by "shifting" the energy calibration of the data by 350 keV. The resulting energy spectra are shown in Figure 4.8. Although this procedure is intellectually unsatisfying, the beta-particle energy spectrum is an inherent characteristic of the decay and must be reproduced by the calculation to make the comparison of calculated and experimental proton energy shifts meaningful.

Having 'forced' the calculated and experimentally obtained beta-particle spectra to agree the proton energy shifts can be compared. One final issue remains to be resolved. A consistent procedure for extracting peak centroids must be developed. For the calculated spectra alone the obvious solution is to take the mean of all the counts,

$$\overline{E} = \frac{\sum E_i N_i}{\sum N_i}, \qquad (3.1)$$

where N_i and E_i are the number of counts and energy corresponding to each channel in the spectra, respectively. The error in this centroid is the standard deviation of the mean,

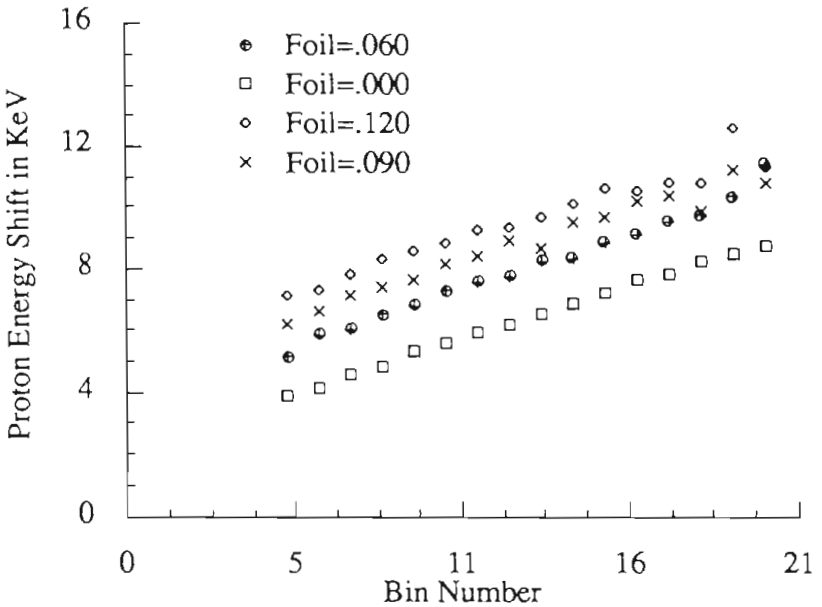

Section 4.7. Calculated proton energy shifts for different counting cell wall thicknesses. The thickness is expressed as the energy loss of a 3.2 MeV proton passing normally through the foil. The actual energy loss in the foil used was 82.6 ± 1.0 keV.

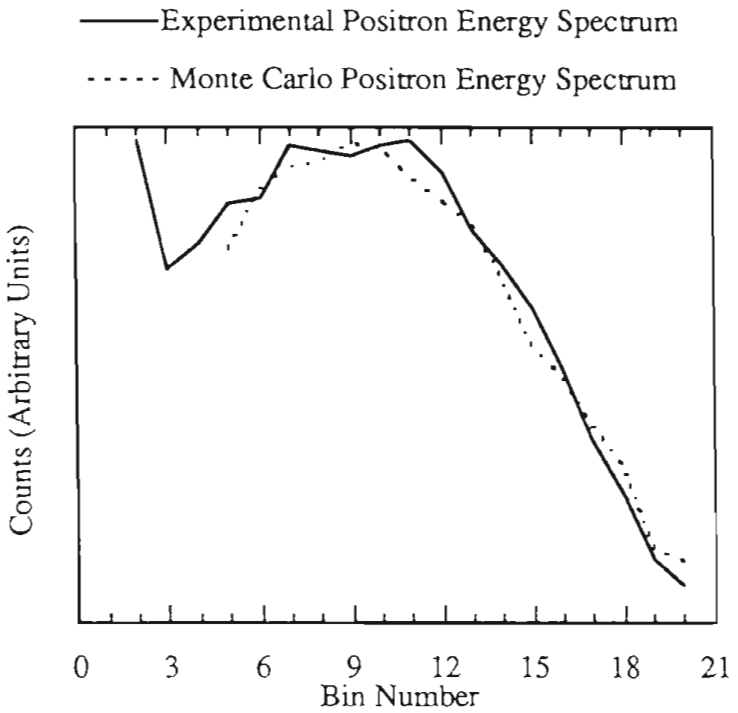

Figure 4.8. Detected and calculated positron energy spectra. Each bin corresponds to a 250 keV range of positron energy.

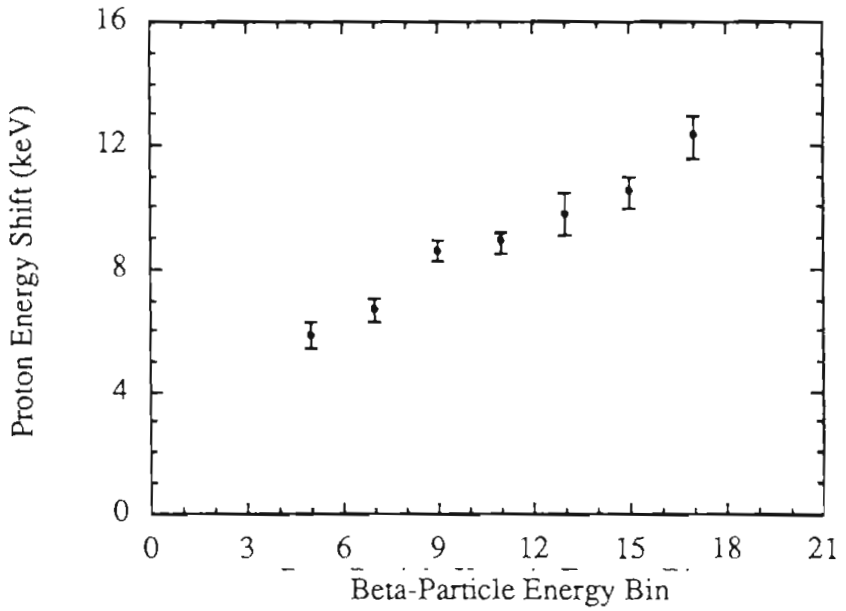

Figure 4.9. Experimental proton energy shifts as a function of beta-particle energy bin. Each bin represents a range of 500 keV in detected beta-particle energy; positrons with energies between 0 keV and 500 keV contribute to bin number one.

Table 4.2. Experimental proton energy shifts for each positron energy bin.

Positron Energy Bin (MeV)	Proton Energy Shift (keV)
1.0 to 1.5	5.8 ± 0.4
1.5 to 2.0	6.7 ± 0.4
2.0 to 2.5	8.6 ± 0.4
2.5 to 3.0	8.9 ± 0.4
3.0 to 3.5	9.8 ± 0.7
3.5 to 4.0	10.5 ± 0.5
4.0 and over	12.3 ± 0.7

$$\sigma_{\bar{E}} = \frac{\sigma_E}{\sqrt{N}}, \qquad (3.2)$$

where N is the total number of counts and σ_E is the standard deviation of the distribution.

This method is difficult to apply to the experimental spectra. Background and beta-decay strength to states nearly degenerate with the analog state can introduce considerable systematic error to the determination of the means. There is no evidence of significant beta-decay strength to a state near the analog, but unfortunately an appreciable background was collected with the valid events. The dependence of this background on energy is not known, but it is greater on the low-energy side of the peak. In spite of this, centroids have been extracted using equation 4.1 on a (carefully selected) 100-keV wide region around the maximum of the peak. These are the results plotted in Figure 4.9. and listed in Table 4.2.

An alternative to employing Equation 4.1 is to attempt to fit the peaks and compare measures of central tendency produced by the fits. This approach has the advantage that the parameters of the fit are determined primarily by the majority of the counts which lie in the main body of the peak. The determination of the centroid is therefore not held hostage to counts in the tails. The principle disadvantage to fitting is that the functional forms of the peak and background are not known. It is possible to obtain a 'good' fit for the data by assuming, for instance, a parabolic background and a Gaussian peak shape. This fit however will produce grossly inaccurate peak centroids.

A second drawback to fitting is that the shapes of the peaks appear to vary between calculated and experimental spectra and also between perpendicular and antiparallel spectra. The latter variation is an effect of energy loss of protons in the gas cell wall. The distributions of angles at which the two sets of protons traverse the wall

are different, and the perpendicular spectra are roughly 10% wider than the antiparallel. It is not certain why the calculated and experimental spectra appear to have different shapes, but this seems to be an illusion caused by the low statistics and background of the experimental spectra. The form of the sum of all the experimental spectra is similar to that of the calculated spectra.

Our ignorance of the functional forms of the peaks and backgrounds and the variations of these forms make comparisons of the calculated and experimental shifts difficult. Arguments that systematic errors are introduced through the fits can not be refuted easily. Several fitting procedures in extracting measures of central tendency of data as well as the calculations have been attempted.

The first function to be employed was a simple Gaussian. This function clearly could not reproduce the spectra, since the peaks are asymmetric. It was suspected, however, that such a fit might produce comparable quantities. This was not the case; the fits to the experimental spectra centered the Gaussian near the mode of the experimental spectra, while the fits of the simulation placed the Gaussian on the order of 1-keV lower in energy.

An attempt was made to fit a Gaussian with a quadratic background. Again, comparable quantities could not be extracted reliably, since the fitting routine would compensate for the tail in the peak differently for the calculation and data.

The last and most promising function fitted was a skewed Gaussian with a linear background. In this function the argument of the exponential of a simple Gaussian is replaced by

$$\frac{(x-\bar{x})^2}{2\sigma^2} \rightarrow \frac{(x-\bar{x})^2}{2(\sigma + s(x-\bar{x}))^2} \tag{4.3}$$

where the parameters of the fit are the width σ, skew s, and mode x. Comparisons of the modes is an improvement over the fitting procedures discussed above, however it should be noted that even here the varying shapes of the experimental distributions make these results less reliable. The results of this procedure are shown in Figure 4.10.

Section 4.5. Comparison of the Calculations and Data.

Figures 4.10 and 4.11 show comparisons of proton energy shifts extracted from the experimental and simulated spectra. Two statements should be made. First, the determination of *a* will be statistics limited. Second, the low-beta-energy bins of the data tend to lie below the line formed by the calculations while the reverse is true for the high energy bins. The latter observation has come to be known as the 'slope problem'. It is possible that the lowest-beta-energy bin, bin 5, has been contaminated by accidental coincidences with abundant γ-rays which of course have an average proton-energy shift of zero. The lowest four bins were excluded for just this reason; the presence of contamination was deduced when the shape of the beta-energy spectrum was analyzed. The slope problem may also be an effect of the inadequate background subtraction or an error in the simulation program. The beta-particle response function assumed for the simulation can also reduce the slope of the calculations if the function spreads too many events out of their original bin. The response function however is known to have too small of an effect to solve the slope problem.

Whatever the origin of the differing slopes, the practical effect is to reduce the sensitivity of the comparison of calculated and experimental shifts to the correlation coefficient. As *a* is lowered from 1.00, the interception of the line of the calculated shifts with the line of the data shifts slowly moves to lower bins. The chi-squared function

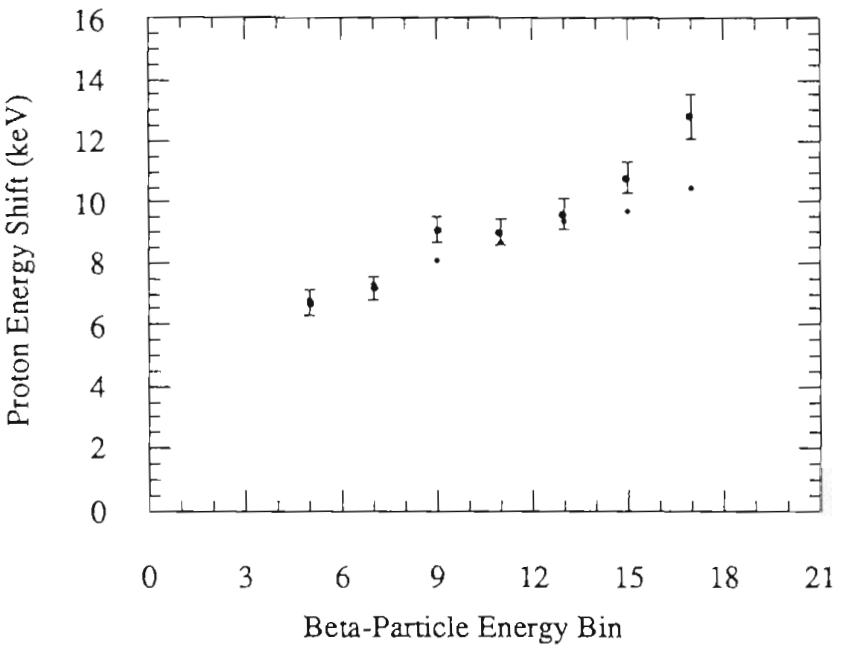

Figure 4.10. Experimental and calculated proton energy shifts as a function of beta-particle energy bin. Each bin represents 500 keV. Peak positions are obtained fitting skewed Gaussians of formula 4.3. The calculation is for $a = 0.92$.

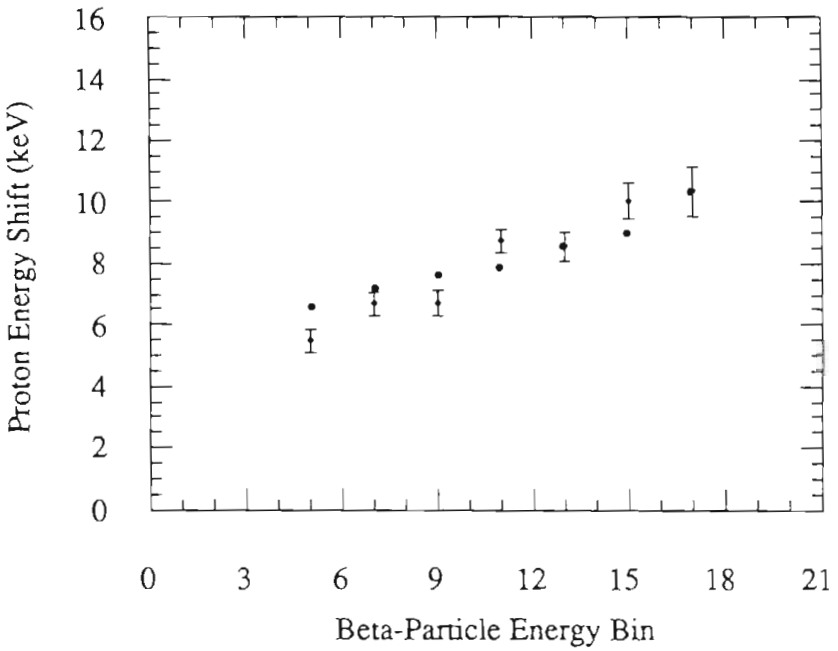

Figure 4.11. Experimental and calculated proton energy shifts as a function of beta-particle energy bin. Each bin represents 500 keV. Peak positions are obtained statistically using formula 4.1 in a 100 keV region around the peak. The calculation is for $a = 0.90$.

passes through only a very broad minimum around $a = 0.90$ as seen on Figure 4.12. This value remains roughly constant for each method of extracting the centroids.

An attempt could be made to circumvent the slope problem by adding all spectra from bins 6 to 20 together and taking the centroids of the total peaks. This approach would succeed if enough statistics had been collected to overcome the broadening of the antiparallel spectrum and the loss of the beta-energy information, however this was not the case.

Section 4.6. Conclusions

At the present state of data analysis and calculations one cannot extract the limits on the angular correlation coefficient which would make existing limits on C_S/C_V tighter. The analysis yields $a = 0.90$, but with an error which is strongly dependent on the method used to extract peaks positions from the data. Due to the slope problem discussed above the chi-squared function has a rather broad minimum as a function of a. A rough estimate of the error in the value of a derived from data like those shown in Figure 4.12 gives $\Delta a = 0.05$.

The following are possible reasons for the disagreement between the results of Monte Carlo modeling and the data. First, there is possibly software error in the Monte Carlo code, which despite numerous efforts has escaped detection. The second reason is a possible error in the data sorting routines. The third reason is the possibility that there are some effects in the experiment which have not been properly taken into account in the simulation. One should also stress that having data with better statistics and lower background would help in the data analysis. Better statistics however would not solve the slope problem.

Future attempts to improve on the determination of a must therefore concentrate on solving the problems listed above. With the exception of improving the statistics, there are no easy solutions in sight, however. In the short time scale one should continue testing the Monte Carlo code. Until the slope problem is understood it does not seem appropriate to suggest repeating the experiment with better statistics.

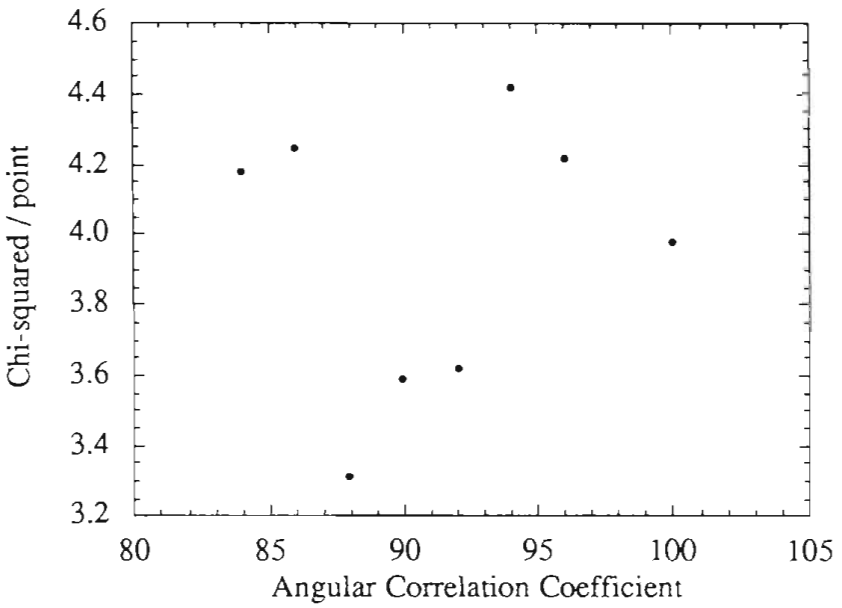

Figure 4.12. Chi-squared per point for various values of the angular correlation coefficient.

Chapter 5. Discussion and Conclusions.

Section 5.1. The Measurement of *a*.

In an attempt to improve the limit of the ratio of scalar to vector interaction strengths we have measured the angular correlation of the superallowed beta-decay of ^{33}Ar. The experiment was performed by measuring the energy shift between delayed-protons emitted at 90° and 180° relative to the direction of emission of the coincident positrons. Since the energy shift is due to the recoil velocity of the ^{33}Cl atom, the shift is a function of the positron energy and the angular correlation coefficient. The extraction of the coefficient consisted of comparing the experimental energy shifts with shifts generated by Monte Carlo simulation of the experiment performed for various values of *a*. The best value obtained is 0.90 ± 0.05.

To extract the scalar interaction strength for this decay the Fermi and Gamow-Teller transition strengths must be estimated. Shell model calculations indicate that the ratio of Gamow-Teller to Fermi strength is 0.053 ± 0.007. The coupling constant ratio g_A/g_V is taken from comparisons of data on Gamow-Teller transition strengths to global shell model calculations of the same quantity, yielding $\left|\frac{g_A}{g_V}\right| = 0.95 \pm 0.04$. With these assumptions the scalar to vector interaction strength is limited by the above value of *a* to be

$$(g_S/g_V)^2 \leq 0.067.$$

The correlation coefficient also places a limit on the Gamow-Tell to Fermi transition strength ratio. Assuming the scalar interaction coupling constant is zero and applying Equation 2.24, we find

$$B(GT) / B(F).= 07 \pm .04,$$

which is consistent with the value resulting from the most recent global shell model wave functions,

$$\frac{B(GT)}{B(F)} = 0.060 \text{ (Bro85) and } 0.046 \text{ (Mul84).}$$

Section 5.2. Conclusions.

In the experiment described in this thesis we have measured for the first time beta-neutrino angular correlations in the decay of 33Ar. This is only the third system in which delayed-particle emission is used to determine the correlations, and the first in which delayed-proton emission was used. However, the project was not as successful as initially expected. The main problem limiting the accuracy of the obtained angular correlation coefficient is the persistent disagreement between the data and the Monte Carlo modeling of the experiment. This disagreement makes the precise determination of a impossible at this time.

References

(All59) J.S. Allen, R.L. Burman, W.B. Herrmannsfeldt, P. Stahelin, and T. Braid, Phys. Rev. **116**, 134 (1959).

(Ays85) J. Aysto, D.M. Moltz, X.J. Xu, J.E. Reiff, and J. Cerny, Phys. Rev. Lett. **55**, 1384 (1985).

(Bar58) C.A. Barnes, W.A. Fowler, H.B. Greenstein, C.C. Lauritsen, and M.E. Nordberg, Phys. Rev. Lett. **1**, 328 (1958).

(Bec96) H. Becquerel, Comptes Rendus **122**, 501 (1896)

(Bec00) H. Becquerel, Comptes Rendus **130**, 809 (1900)

(Bet53) H.A. Bethe and J. Ashkin, in *Experimental Nuclear Physics*, ed. E. Segré, (Wiley, New York, 1953).

(Bli69) R.J. Blin-Stoyle, in *Isospin in Nuclear Physics*, ed. D.H. Wilkinson (North-Holland 1969) chap. 4.

(Bon78) L.N. Bondarenko, V.V. Kurguzov, Y.A. Prokof'ev, E.V. Rogov, and P.E. Spivak, Pis'ma Zh. Eksp. Teor. Fiz. **28**, 328 (1978) [JETP Lett. **28**, 303 (1978)].

(Boo84) A.I. Boothroyd, J. Markey, and P. Vogel, Phys. Rev **C29**, 603 (1984).

(Bor87) M.J.G. Borge, P. Dessagne, G.T. Ewan, P.G. Hansen, A. Huck, B. Jonson, G. Klotz, A. Knipper, S. Mattsson, G. Nyman, C. Richard-Serre, K. Riisager, G. Walter, and the ISOLDE Collaboration, Phys. Scr. **36**, 218 (1987).

(Bor86) M.J.G. Borge, M. Epherre-Rey-Campagnolle, D. Guillemaud-Mueller, B. Jonson, M. Langevin, G. Nyman, C. Thibault, and the ISOLDE Collaboration, Nucl. Phys. **A460**, 373 (1986).

(Bor87) V. Borrel, J.C. Jacmart, F. Pougheon, A. Richard, Nucl. Phys. **A473**, 331 (1987).

(Bro85) B.A. Brown and B.H. Wildenthal, ADNDT **33**, 347 (1985).

(Bur60) M.T. Burgy, V.E. Krohn, T.B. Novey, G.R. Ringo, and V.L. Telegdi, Phys. Rev. **120**, 1829 (1960).

(Byr80) J. Byrne, J. Morse, K.F. Smith, F. Shaikh, K. Green, and G.L. Greene, Phys. Lett. **92B**, 274 (1980).

(Cab83) M.D. Cable, J. Honkanen, R.F. Parry, S.H. Zhou, Z.Y. Zhou, and J. Cerny, Phys. Rev. Lett. **50**, 404 (1983).

(Car63) T.A. Carlson, Phys. Rev. **132**, 2239 (1963).

(Chr72) C.J. Christensen, A. Nielsen, A. Bahnsen, W.K. Brown, and B.M. Rustad, Phys. Rev. D **5**, 1628 (1972).

(Chu76) W. Chung, Ph.D. Thesis (Michigan State University, 1976).

(Cli89) E.T.H. Clifford, E. Hagberg, J.C. Hardy, H. Schmeing, R.E. Azuma, H.C. Evans, V.T. Koslowsky, U.J. Schrewe, K.S. Sharma, and I.S. Towner, Nucl. Phys.**A493**, 293 (1989).

(Com83) E.D. Commins and P.H. Bucksbaum, *Weak Interactions of Leptons and Quarks* (Cambride University Press, Cambridge, 1983).

(Dob75) R. Dobrozemsky, E. Kerschbaum, G. Moraw, H. Paul, C. Stratowa, and P. Weinzierl, Phys. Rev. D **11**, 510 (1975).

(Est71) J.E. Esterl, R.G. Sextro, J.C. Hardy, G.J.Ehrhardt, and J. Cerny, NIM **97**, 229 (1971).

(Fer50) E. Fermi, Nucl. Phys., Notes compiled by J. Orear, A.H. Rosenfeld, and R.A. Schluter, Univ. of Chicago Press, Chicago, Ill, (1950).

(Fey58) R.P. Feynman and M. Gell-Mann, Phys. Rev. **109**, 193 (1958).

(Geo84) H. Georgi, *Weak interactions and Modern Particle Theory* (Benjamin/Cummings, Menlo Park, CA, 1984).

(Gla61) S.L. Glashow, Nucl. Phys. **22**, 579 (1961).

(Gla70) S.L. Glashow, J. Iliopoulos, L. Maiani, Phys. Rev. D **2**, 1285 (1970).

(Gol58) M. Goldhaber, L. Grodzins, and A.W. Sunyar, Phys. Rev. **109**, 1015 (1958).

(Gri68) V.K. Grigor'ev, A.P. Grish(in, V.V. Vladimirskii, E.S. Nikolaevskii, and D.P. Zharkov, Sov. J. Nucl. Phys. **6**, 239 (1968)

(Hal84) F. Halzen and A.D. Martin, *Quarks and Leptons* (John Wiley & Sons, New York, 1984).

(Har70) J.C. Hardy, J.E. Esterl, R.G. Sextro, and J. Cerny, Phys. Rev. C **3**, 700 (1971).

(Har74) J.C. Hardy, in *Nuclear Spectroscopy and Reactions*, part C, ed. J. Cerny (Academic Press, 1974) chap. VIII.B.

(Her57) W.B. Herrmannsfeldt, D.R. Maxson, P. Stahelin and J.S. Allen, Phys Rev **107**, 641 (1957).

(Hig64) P.W. Higgs, Phys. Lett. **12**, 132 (1964).

(Hol74) B.R. Holstein, Rev. Mod. Phys. **46**, 789 (1974).

(Hon83) J. Honkanen, M.D. Cable, R.F. Parry, S.H. Zhou, Z.Y. Zhou, and J. Cerny, Phys. Lett. **133B** 146 (1983).

(Iko73) P.G. Ikossi, Program BABEL, TUNL 1973, unpublished.

(Iko75) P.G. Ikossi, Ph.D. Thesis (The University of North Carolina at Chapel Hill, 1976).

(Jam75) F. James and M. Roos, Comp. Phys. Comm. **10**, 343 (1975).

(Joh63) C.H. Johnson, F. Pleasonton, and T.A. Carlson, Phys. Rev. **132**, 1149 (1963).

(Kob73) M. Kobayashi and T. Maskawa, Prog. Theor. Phys. (Japan) **49**, 652 (1973).

(Lau58) T. Lauritsen, C.A. Barnes, W.A. Fowler, and C.C. Lauritsen, Phys. Rev. Lett. **1**, 326 (1958).

(Led78) C.M. Lederer and V.S. Shirley, ed., *Table of Isotopes* (Wiley, New York, 1978).

(Mac71) R.D. MacFarlane, N.S. Oakey, and R.J. Nickles, Phys. Lett. **34B**, 133 (1971).

(Mul84) W. Muller, B.C. Metsch, W. Knupfer, and A. Richter, Nucl. Phys **A430**, 61 (1984).

(Pau70) H. Paul, Nucl. Phys. **A154**, 160 (1970).

(Ram78) S. Raman, C.A. Houser, T.A. Walkiewicz, and I.S. Towner, ADNDT **21**, 567 (1978).

(Rid61) B.W. Ridley, Nucl. Phys. **25**, 483 (1961).

(Rob58) J.M. Robson, Can. J. Phys. **36**, 1450 (1958).

(Rus53) B.M. Rustad and S.L. Ruby, Phys. Rev. **90**, 370 (1953).

(Rus55) B.M. Rustad and S.L. Ruby, Phys. Rev. **97**, 991 (1955).

(Sak67) J.J. Sakurai, *Advanced Quantum Mechanics* (Addison-Wesley, Reading, Mass., 1967).

(Sal64) A. Salam and J.C. Ward, Phys. Lett. **13**, 168 (1964).

(Sch66) H.F. Schopper, *Weak Interactions and Nuclear Beta Decay* (North-Holland, Amsterdam, 1966).

(Tem74) G.M. Temmer, in *Nuclear Spectroscopy and Reactions*, part B, ed. J. Cerny (Academic Press, 1974) chap. IV.B.

(Thi78) W. G. Thies, H. Appel, and H. Behrens, Phys. Lett. **73B**, 411 (1978).

(Tre59) Y.V. Trebukhovskii, V.V. Vladimirskii, V.K. Grigor'ev, and V.A. Ergakov, Sov. phys. - JETP **9**, 931 (1959).

(Vis63) J.B. Vise and B.M. Rustad, Phys. Rev. **132**, 2573 (1963).

(Wei67) S. Weinberg, Phys. Rev. Lett. **19**, 1264 (1967).

(Wei70) S. Weinberg, Phys. Rev. D **5**, 1412 (1972).

(Wil73) D.H. Wilkinson, Nucl. Phys. A **209**, 470 (1973).

(Wil78) D.H. Wilkinson, A. Gallmann and D.E. Alburger, Phys Rev. **C18**, 401 (1978).

(Wil82) D.H. Wilkinson, Nucl Phys **A377**, 474 (1982).

(Wil84) B.H. Wildenthal, *Progress in Particle and Nuclear Physics*, Vol. 11, ed. by D.H. Wilkinson (Pergamon Press, Oxford, 1984), p 5.

(Wu57) C.S. Wu, E. Ambler, R.W. Hayward, D.D. Hoppes, and R.P. Hudson, Phys. Rev. **105**, 1413 (1957).

(Wu66) C.S. Wu and S. A. Moszkowski, *Beta Decay* (Interscience Publishers, London, 1966)